J. Fluid Mech. (2012), *vol.* 712, *pp.* 92–128.
doi:10.1017/jfm.2012.403

Coherent structures and associated subgrid-scale energy transfer in a rough-wall turbulent channel flow

Jiarong Hong[1], Joseph Katz[1]†, Charles Meneveau[1] and Michael P. Schultz[2]

[1] Johns Hopkins University, Baltimore, MD 21218, USA

[2] United States Naval Academy, Annapolis, MD 21402, USA

(Received 15 January 2012; revised 19 July 2012; accepted 6 August 2012;
first published online 27 September 2012)

This paper focuses on turbulence structure in a fully developed rough-wall channel flow and its role in subgrid-scale (SGS) energy transfer. Our previous work has shown that eddies of scale comparable to the roughness elements are generated near the wall, and are lifted up rapidly by large-scale coherent structures to flood the flow field well above the roughness sublayer. Utilizing high-resolution and time-resolved particle-image-velocimetry datasets obtained in an optically index-matched facility, we decompose the turbulence into large ($>\lambda$), intermediate (3–6k), roughness (1–3k) and small ($<k$) scales, where k and $\lambda(\lambda/k = 6.8)$ are roughness height and wavelength, respectively. With decreasing distance from the wall, there is a marked increase in the 'non-local' SGS energy flux directly from large to small scales and in the fraction of turbulence dissipated by roughness-scale eddies. Conditional averaging is used to show that a small fraction of the flow volume (e.g. 5 %), which contains the most intense SGS energy transfer events, is responsible for a substantial fraction (50 %) of the energy flux from resolved to subgrid scales. In streamwise wall-normal (x–y) planes, the averaged flow structure conditioned on high SGS energy flux exhibits a large inclined shear layer containing negative vorticity, bounded by an ejection below and a sweep above. Near the wall the sweep is dominant, while in the outer layer the ejection is stronger. The peaks of SGS flux and kinetic energy within the inclined layer are spatially displaced from the region of high resolved turbulent kinetic energy. Accordingly, some of the highest correlations occur between spatially displaced resolved velocity gradients and SGS stresses. In wall-parallel x–z planes, the conditional flow field exhibits two pairs of counter-rotating vortices that induce a contracting flow at the peak of SGS flux. Instantaneous realizations in the roughness sublayer show the presence of the counter-rotating vortex pairs at the intersection of two vortex trains, each containing multiple λ-spaced vortices of the same sign. In the outer layer, the SGS flux peaks within isolated vortex trains that retain the roughness signature, and the distinct pattern of two counter-rotating vortex pairs disappears. To explain the planar signatures, we propose a flow consisting of U-shaped quasi-streamwise vortices that develop as spanwise vorticity is stretched in regions of high streamwise velocity between roughness elements. Flow induced by adjacent legs of the U-shaped structures causes powerful ejections, which lift these vortices away from

† Email address for correspondence: katz@jhu.edu

the wall. As a sweep is transported downstream, its interaction with the roughness generates a series of such events, leading to the formation of inclined vortex trains.

Key words: boundary layer structure, channel flow, turbulent boundary layer

1. Introduction

Turbulence is commonly described in terms of interactions among flow structures of a hierarchy of length scales that exchange kinetic energy in a cascading process. In wall-bounded flows, these structures are strongly affected and constrained by boundary conditions. In smooth-wall boundary layer and channel flows, the most relevant characteristic length scales are the viscous wall unit, δ_υ, which represents the effect of wall stress, and the integral scale, i.e. the boundary layer thickness, δ, or half-channel height, h (Pope 2000). In rough-wall boundary layers, there are also characteristic scales associated with the topography of the rough surface, e.g. the height of individual roughness elements, k, their surface density, etc. (Jiménez 2004). Typically, these roughness scales fall between the wall unit and integral length scale. The roughness embeds its signature through interactions with the turbulence and dominates the near-wall flow structure. To resolve rough-wall turbulence using direct numerical simulation (DNS), the computational grid has to be of the order of δ_υ, and should resolve the flow around individual roughness elements. In addition, to capture the large-scale structures in the flow requires a computational domain of the order of δ or h. Consequently, the present DNS cannot be applied under high Reynolds number and fully rough flow conditions. To cope with this limitation, large eddy simulation (LES) resolves only the large-scale structures, but still has to model the subgrid-scale (SGS) physics, including near-wall flow phenomena associated with turbulence–roughness interactions (Piomelli 2008). Due to the diversity of roughness configurations, one of the key issues in modelling rough-wall turbulence is to define proper roughness scales based on the surface geometry, and to quantify their influence on the turbulence in a general manner.

Substantial work has focused on specifying the boundary conditions to parametrize the effect of roughness as an additional momentum flux (drag force). A common approach utilizes the Monin–Obukhov similarity theory (Monin & Obukhov 1959), which leads to a law-of-the-wall above the roughness in neutral turbulent flows. This method requires a specified roughness scale and displacement height to represent the aggregate effects of unresolved surface details, mostly the form drag induced by the roughness. Numerous studies (e.g. Avissar & Pielke 1989; Bou-Zeid, Meneveau & Parlange 2004; Chamecki, Meneveau & Parlange 2009; Anderson & Meneveau 2010) have applied and extended this approach to achieve reasonable prediction of the drag and mean velocity profile on various rough surfaces. Nevertheless, due to lack of information on the relationship between the instantaneous wall stress (form drag) and resolved flows, these predictions inevitably involve *ad hoc* assumptions, which limit their accuracy and robustness. Another issue is related to the challenges of SGS stress modelling near the roughness, where LES inherently under-resolves the energy-containing motions at the first few grid cells, therefore producing localized error in resolved velocity (Juneja & Brasseur 1999). Such errors would be of minor consequence if their influence were confined to the near-wall region. However, since they affect the mean momentum flux and the region of peak energy production,

their effects propagate throughout the entire flow. Furthermore, under more general conditions, such as in buoyancy-affected boundary layers, Khanna & Brasseur (1998) show that these errors can be carried upward by buoyancy-driven vertical fluxes. Our recent publication (Hong, Katz & Schultz 2011) also shows that in a channel flow, the roughness-scale eddies are lifted up rapidly by the outer-layer structures, flooding the entire boundary layer with small-scale energy. Accounting for the excess kinetic energy associated with these structures imposes a challenge to the modelling of SGS dynamics. To develop fresh modelling strategies, we need to understand how small-scale structures are generated and transported away from the wall, how they interact with resolved-scale eddies, and how they impact the SGS energy fluxes.

Constrained by experimental techniques and computational capacity, only a few studies have focused on the flow structure and turbulence in the inner part of rough-wall boundary layers, commonly referred to as the roughness sublayer. Recently, DNS of a turbulent channel flow over two-dimensional ribs by Ikeda & Durbin (2007) has revealed that disruption of three-dimensional vortical streaks in the roughness sublayer is responsible for high energy production just above the roughness. For a similar rough surface configuration, Lee & Sung (2007) report a significant effect of roughness on the redistribution of turbulent kinetic energy (TKE) near the wall. A subsequent DNS by Lee, Sung & Krogstad (2011) compares the near-wall structures over two-dimensional and three-dimensional roughness with those of smooth walls, showing that in the presence of roughness, the streamwise structures are shorter and ejections are more vigorous. The particle-image-velocimetry (PIV) measurements of Djenidi *et al.* (2008) reveal that roughness-scale spanwise vortices originating at the trailing edge of the roughness elements are convected downstream and strongly interact with the overlying turbulent flow. Our PIV measurements (Hong *et al.* 2011) show that in the roughness sublayer the mean flow, Reynolds stresses, and TKE budget terms display significant spatial variability, and that the production rate peaks above the frontal face of roughness elements.

For high Reynolds number flows above the roughness sublayer, Raupach, Antonia & Rajagopalan (1991) extend Townsend's (1976) similarity hypothesis by proposing that turbulent motions normalized by friction velocity are independent of wall roughness. Numerous studies, too many to summarize here, have examined the validity of this hypothesis. For example, strong support has been provided by Bandyopadhyay & Watson (1988) and Schultz & Flack (2003). Conversely, some other studies, e.g. Krogstad, Antonia & Browne (1992), Krogstad & Antonia (1999), Tachie, Bergstrom & Balachandar (2000, 2003) and Keirsbulck *et al.* (2002), have observed significant roughness-dependent changes to the Reynolds stresses that extend well into the outer layer. A detailed review by Jiménez (2004) points out that the conflicting evidence is related to the differences in scale separation, i.e. δ/k and $k^+ = kU_\tau/\nu$, where U_τ is the friction velocity and ν is the kinematic viscosity. To obtain a 'well-characterized' rough-wall turbulent boundary layer for examining the similarity hypothesis, both k^+ and δ/k must exceed threshold values, typically $k^+ > 50$–100 and $\delta/k > 40$, and their product, i.e. δ^+, should be at least 4000. Following this guidance, recent experiments (e.g. Flack, Schultz & Shapiro 2005; Kunkel & Marusic 2006; Schultz & Flack 2007; Wu & Christensen 2007, 2010) have shown strong support for similarity in the outer layer. With a few exceptions, most of the rough-wall studies have inferred the characteristics of turbulence structures through statistics, such as Reynolds stresses and higher-order moments. However, a number of recent studies have attempted to examine the scale and alignment of coherent structures in the outer layer, through two-point correlations, proper orthogonal decomposition (POD), and conditional averaging using

linear stochastic estimation (LSE), for example. For two-point correlations of both streamwise and wall-normal velocity components as well as quadrant analysis results, excellent agreement with smooth wall data has been found by Wu & Christensen (2007). Applying POD, their subsequent study (Wu & Christensen 2010) indicates that large-scale fields are sensitive and small scales are insensitive to roughness effects. Volino, Schultz & Flack (2007) also demonstrate a close agreement with smooth-wall turbulence in energy spectra, the probability density function of swirling strength and two-point correlations. Moreover, their two-dimensional PIV data display vortical patterns with features similar to those described by the popular hairpin packet model for smooth walls (Adrian, Meinhart & Tomkins 2000). However, spatial energy spectra presented in our recent work (figure 1, Hong *et al.* 2011) and in Hackett *et al.* (2011) show that the turbulence contains an excessive amount of energy at scales corresponding to k well above the roughness sublayer. Although they do not have a significant effect on the Reynolds stresses, they influence the dissipation rate in the outer layer.

The present paper focuses on the role of coherent structures in SGS energy transfer, a topic investigated in several prior studies by applying conditional averaging. Using DNS data for low Reynolds number ($Re_\tau = 180$) smooth-wall channel flow, Piomelli, Yu & Adrian (1996) showed that the near-wall, inter-scale energy transfer is strongly correlated with the presence of coherent structures. They found that strong positive (forward scatter) and negative (backward scatter) SGS energy fluxes are induced by the same quasi-streamwise or hairpin vortices. In a field experiment using sonic anemometry, Carper & Porté-Agel (2004) revealed vortical structures that are conceptually consistent with the hairpin model, which generate both forward and backward scatter in different parts of the same structure. Recently, combining conditional averaging and observation of instantaneous realizations for PIV data in a smooth-wall boundary layer, Natrajan & Christensen (2006) have shown that strong SGS energy transfer is associated with organized hairpin packets. They observe that strong forward scatter events exist between consecutive hairpin heads while strong backward scatter occurs at the trailing edge of the vortex packets.

To further investigate this subject and elucidate the interactions between coherent structures over rough walls, in the present work we apply spatial filters to decompose the flow into relevant scale ranges and measure the associated inter-scale energy fluxes. Subsequently, conditional averaging, combined with observations in the time-resolved data, is used to identify flow structures that dominate the energy fluxes. We find that specific coherent structures play a key role, and that a fraction, e.g. 5 %, of the flow produces more than 50 % of the positive energy flux. The configuration and mechanisms involved in the generation of these structures, along with implications for SGS modelling in LES, are discussed subsequently.

2. Experimental set-up and methodology

2.1. *Facility and measurements*

The experiments were performed in the bypass channel of the Johns Hopkins University optically index-matched test facility. The entire facility was filled with a 62 % by weight solution of sodium iodide (NaI) in water, with refractive index matching that of the acrylic rough walls. This enabled us to conduct PIV measurements very near the surface, including the space between the roughness elements. A brief description of this facility is provided here for clarity, and further details are available in Hong *et al.* (2011). The transparent acrylic channel is 3.3 m

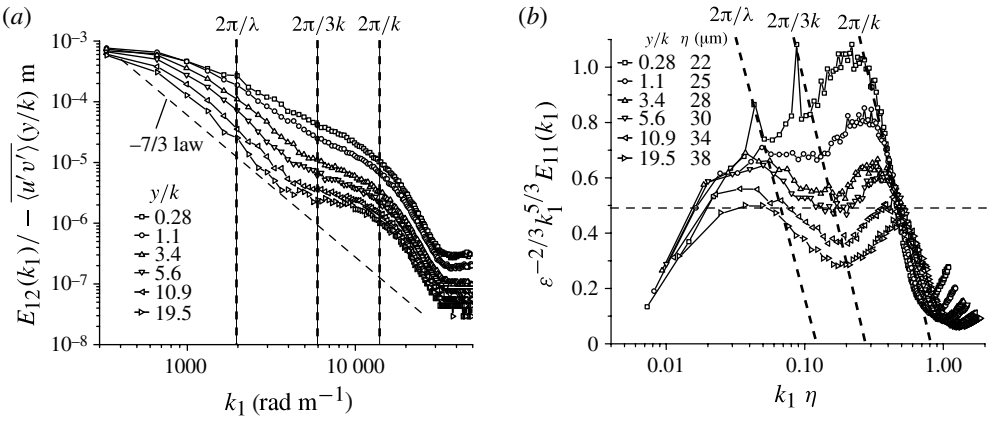

FIGURE 1. (*a*) $E_{12}(k_1)$ scaled by the local shear stress at $y/k = 0.28, 1.1, 3.4, 5.6, 10.9$ and 19.5. (*b*) Compensated $E_{11}(k_1)$ at the same elevations. The horizontal dashed line shows the values for inertial-range isotropic turbulence. The vertical dashed lines in (*a*) and inclined lines in (*b*) mark the wavenumbers corresponding to length scales of k, $3k$ and λ.

long and has a 20 cm × 5 cm rectangular cross-section, which facilitates optical access to any internal site from various viewing angles. The channel contains two pairs of 1.25 m long removable acrylic inserts, allowing easy adjustment of the wall properties. The present experiment is installed with a pair of smooth inserts in the upstream half of the channel, and a pair of rough ones downstream. The measurements are carried out at $35h$ from the leading edge of downstream inserts (figure 2*a*), where the turbulence is fully developed and the transition effect from smooth to rough inserts becomes negligible. The surface roughness consists of closely packed, square pyramidal elements with height of $k = 0.46$ mm and wavelength of $\lambda = 3.2$ mm ($\lambda/k = 6.8$), as illustrated in figure 2(*b,c*). For this geometry, the equivalent sand roughness height k_s is about $1.5k$ (Schultz & Flack 2009). Based on the friction velocity ($U_{\tau-uv}$, see table 1) measured by extending the total shear stress to the wall, our flow yields $h/k > 50$ and $k_s^+ > 80$, satisfying the well-characterized condition proposed by Jiménez (2004). The mean velocity profile has a logarithmic shape at $2k < y < 0.2h$, and clearly deviates from it below $y = 2k$ (Hong *et al.* 2011).

The data used in the current paper mainly come from the high-resolution PIV measurements and recently performed time-resolved measurements. The sample areas are indicated in figure 2(*b,c*), and relevant parameters such as centreline velocity U_c and resolution are summarized in table 1. The high-resolution data described in Hong *et al.* (2011) are recorded using a 4864 × 3248 pixel CCD camera. The interrogation window size is 32 × 32 pixels, which with 50 % overlap provides a vector spacing of 63 μm, i.e. $\sim 0.14k$. The time-resolved PIV measurements use a high-speed CMOS camera, PCO Dimax, with a maximum sensor area of 2048 × 2048 pixels when running at 1 kHz. In order to achieve both sufficient time and spatial resolution for resolving the evolution of turbulence structures, the active sensor area in the x–y plane measurement is reduced to 1344 × 704 pixels to increase the camera speed to 5 kHz. The field of view is about 4λ in the streamwise direction, and extends from below the crest of the pyramids to $12k$ above (figure 1*c*). Data have been obtained in two x–y planes, the same as in the high-resolution measurement, one aligned with crest lines of the pyramids and the other plane between them.

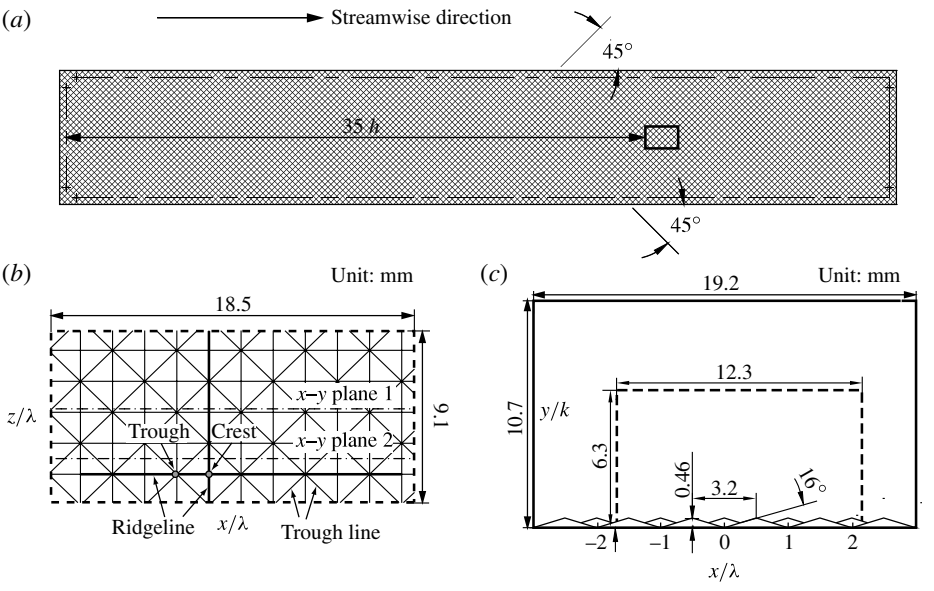

FIGURE 2. (*a*) The rough insert plate showing the measurement region marked with a rectangle. (*b*) The *x*–*z* sample areas of time-resolved (dashed rectangle) measurements along with the location of *x*–*y* measurement planes. (*c*) The *x*–*y* sample areas of high resolution (solid rectangle) and time-resolved (dashed rectangle) measurements.

Using a pulsed laser generating pairs of exposures with in-pair delay of 80 μs at 2.5 kHz, and frame straddling to record each exposure on a different frame, we obtain a 2.5 kHz time series of velocity distributions. With 50 % overlap between interrogation windows, the vector spacing is 147 μm ($\sim 0.3k$) for this dataset. The measurements in two *x*–*z* planes located at $y = k$ and $11k$ are performed using a lower time resolution, i.e. 800 μs (1.25 kHz), in order to cover a larger field of view. The location and size of this sample area is marked in figure 2(*b*). This time resolution still enables us to observe and follow the development of flow structures in the sample area at this plane over several frames. To track large structures over longer periods, we also record *x*–*y* plane data at 1.25 kHz with a field of view that extends to $\sim 17.1\lambda$ horizontally and covers the entire bottom half of the channel with a vector spacing of 437 μm. Each dataset in both *x*–*y* and *x*–*z* planes contains at least 100 time sequences with 60 continuous vector maps in each sequence. The delay between sequences is long enough to make them statistically independent.

2.2. *Data analysis methodology*

2.2.1. *Selection of filter scales*

Two-dimensional top-hat filtering is applied to spatially filter the original velocity field using the filter sizes indicated in table 1. The filter sizes are selected based on the characteristics of the spatial shear and compensated energy spectra taken from Hong *et al.* (2011) and shown in figure 1. Each of these spectra is calculated by applying fast Fourier transforms to instantaneous data obtained along streamwise lines and then averaging them for all 5000 realizations. The spatial shear spectra in figure 1(*a*) are scaled by the spatially averaged Reynolds stress at the corresponding elevation, while keeping both horizontal and vertical axes dimensional. This scaling emphasizes

https://doi.org/10.1017/jfm.2012.403 Published online by Cambridge University Press

Orientation and location	Acquisition rate	U_c (m s^{-1})	$U_{\tau-uv}$ (m s^{-1})	Re_τ	Vector spacing (μm)	Field of view (mm)	Filter size
x–y plane, ridgeline	1 Hz	2.75	0.155	3520	63	19 × 11	k, 3k, 6k
x–y plane, ridgeline	2.5 kHz	2.71	0.152	3380	147	12 × 6	3k
x–z plane, $y = k$	1.25 kHz	2.71	0.152	3380	147	19 × 9	3k
x–z plane, $y = 11k$	1.25 kHz	2.71	0.152	3380	147	19 × 9	3k
x–y plane, ridgeline	1.25 kHz	2.71	0.152	3380	437	55 × 26	λ, 2λ

TABLE 1. Flow conditions and datasets used in the current analysis.

subtle variations in shape with increasing distance from the wall. The compensated energy spectra of streamwise velocity components, i.e. $E_{11}(k_1)\varepsilon^{-2/3}k_1^{5/3}$ (E_{11} is the streamwise component of TKE, k_1 is the streamwise wavenumber, and ε is the dissipation rate), shown in figure 1(*b*), are plotted against $k_1\eta$, where $\eta = (\nu^3/\varepsilon(y))^{1/4}$ is the Kolmogorov scale specified in the legend of figure 1(*b*). The dissipation rate is calculated directly from the in-plane velocity gradients. As discussed in Hong *et al.* (2011), the magnitude of dissipation rate is underestimated by ∼50 % due to the spatial resolution limit caused by the thickness (∼0.5 mm) of the laser sheet and/or depth of field of the imaging system (∼0.28 mm). This underestimate would cause a 17 % overestimate of the Kolmogorov scale. We do not correct the values of η because the specific value does not play a role in the present analysis. Since ε decays with increasing elevation, η increases, and, correspondingly, so do the values of $2\pi\eta/\lambda$ and $2\pi\eta/k$.

To justify our selection of filter scales, it is worth reviewing some of the observed spectral features. First, the spectral peak at $k_1 = 2\pi/\lambda$ very near the wall is generated by the periodic spatial variations in the flow within the roughness sublayer. Second, at low wavenumbers, the spectral slope in figure 1(*a*) steepens with increasing distance from the wall, demonstrating a growing contribution of large-scale turbulence and a decreasing role of small-scale energy. Third, in the outer layer, referred to as the region above $10k$ in the following discussion, the shear spectra at low wavenumbers show a tendency towards a $-7/3$ slope, which is the expected value for the inertial-range shear spectrum. Finally, a clear flattening, i.e. a decrease in slope magnitude with increasing distance from the wall, occurs at wavelengths in the 1–3k range. This phenomenon is most pronounced in the presented shear spectra, but is also evident from the distinct bumps in the high wavenumber range of the compensated energy spectra (figure 1*b*). It indicates persistence of excessive roughness-scale (1–3k) energy at all elevations, including well above the roughness sublayer. Similar observations are made in oceanic PIV data, with the bumps appearing at a scale corresponding to the bottom ripple height (Hackett *et al.* 2011).

Another peak forms at low wavenumbers of the compensated $E_{11}(k_1)$ spectra in the vicinity of $k_1\eta \sim 0.04$, i.e. at scales that are slightly larger than the roughness wavelength. With increasing distance from the rough wall, the magnitude of this peak tends towards that of inertial-range isotropic turbulence, which is marked by a horizontal dashed line in figure 2(*b*). The same trend applies to the spectra of the wall-normal velocity component (Hong *et al.* 2011), indicating that turbulence at scales larger than λ tends towards inertial-range behaviour. Thus, it is reasonable to assume that the low wavenumber compensated peak corresponds to the inertial-range structures, while the high wavenumber peak is associated with roughness-scale eddies generated near and amid the roughness elements. Outside of the roughness sublayer, there are clear troughs between the peaks in the compensated spectra that seem to fall approximately at a wavenumber corresponding to $3k$. Based on these observations, we choose three length scales of size $\Delta = k, 3k, 6k$ to filter the original velocity fields. The corresponding lowest resolved frequencies are one half the values marked by the vertical and inclined dashed lines in figure 1(*a,b*), respectively. For example, for a filter with size k, the Nyquist frequency is π/k. They divide the flow field into flow structures in four scale ranges: large ($>6k \sim \lambda$), intermediate (3–6k), roughness (1–3k) and small ($<k$) scales. In addition, two filters of size $\Delta = \lambda$ and 2λ are applied to the low resolution x–y plane data.

2.2.2. *Calculation of SGS turbulence statistics and conditional sampling*

As a preliminary step, we examine trends of SGS stresses and energy fluxes. LES decomposes the flow variables into resolved and unresolved (subgrid-scale) parts by applying a spatial filtering operation (Rogallo & Moin 1984; Lesieur & Metais 1996; Piomelli 1999; Meneveau & Katz 2000). The filtered variable is given by $\tilde{f} = \int_D f(\boldsymbol{x}', t) G_\Delta(\boldsymbol{x}, \boldsymbol{x}')\, \mathrm{d}\boldsymbol{x}'$, where D is the computational domain and G_Δ is the filtering kernel with characteristic scale Δ. The filtered velocity satisfies the filtered momentum equation

$$\frac{\partial \tilde{u}_i}{\partial t} + \tilde{u}_j \frac{\partial \tilde{u}_i}{\partial x_j} = -\frac{\partial}{\partial x_j}\left[\frac{\tilde{p}}{\rho}\delta_{ij} + \tau_{ij}\right] + \nu \frac{\partial^2 \tilde{u}_i}{\partial x_j^2}, \tag{2.1}$$

where $\tau_{ij} = \widetilde{u_i u_j} - \tilde{u}_i \tilde{u}_j$ is the SGS stress. Analysis of the energy budget shows that the energy flux between resolved and unresolved scales, i.e. SGS energy flux, is

$$\Pi^\Delta = -\tau_{ij} \tilde{S}_{ij}, \tag{2.2}$$

where $\tilde{S}_{ij} = 1/2(\partial \tilde{u}_i/\partial x_j + \partial \tilde{u}_j/\partial x_i)$ is the filtered strain rate tensor. The SGS flux when positive appears as a sink term in the kinetic energy equation of filtered velocity and a source in the evolution equation of subgrid kinetic energy. The SGS stress has to be modelled to close the filtered momentum equation. Among the numerous models proposed for the SGS stresses using resolved flow variables, we start by examining two popular models, namely the static Smagorinsky eddy viscosity introduced by Smagorinsky (1963), and the traditional dynamic model (Germano *et al.* 1991; Lilly 1992). Both of them are based on the eddy-viscosity and mixing length assumptions

$$\tau_{ij}^d = -2\nu_T \tilde{S}_{ij}, \quad \nu_T = (C_S \Delta)^2 |\tilde{S}|, \tag{2.3}$$

where $\tau_{ij}^d = \tau_{ij} - 1/3\tau_{kk}\delta_{ij}$ is the deviatoric part of the SGS stress tensor, ν_T is the SGS eddy viscosity, $|\tilde{S}| = (2\tilde{S}_{ij}\tilde{S}_{ij})^{1/2}$, and C_s is the Smagorinsky coefficient. In the static (or dissipation-based) model, C_s is calculated by matching the real and modelled SGS energy fluxes on an average basis, i.e.

$$(C_s)^2 = \langle \Pi^\Delta \rangle / \langle 2\Delta^2 |\tilde{S}| \tilde{S}_{ij} \tilde{S}_{ij} \rangle, \tag{2.4}$$

where $\langle\rangle$ indicates ensemble-averaging. This coefficient guarantees the correct mean depletion of energy from the resolved velocity field. For homogeneous isotropic turbulence, C_s is about 0.16 (Lilly 1967). It should be noted that, limited by the two-dimensional planar data, we cannot calculate the real τ_{ii}^d in the estimate of the Smagorinsky coefficients. Instead, we use τ_{ii}. For incompressible flow ($\tilde{S}_{ii} = 0$), $\langle \tau_{ij}^d \tilde{S}_{ij} \rangle = \langle \tau_{ij} \tilde{S}_{ij} \rangle$, i.e. subtraction of the trace does not affect the overall SGS energy flux. In addition, if the turbulence is isotropic, the subtraction does not even change the average term-wise dissipation, e.g. $\langle \tau_{11}^d \tilde{S}_{11} \rangle = \langle \tau_{11} \tilde{S}_{11} \rangle$, since $\langle \tau_{ii} \tilde{S}_{11} \rangle = 0$, as shown in Meneveau (1994). When the flow is anisotropic at the filtering scale, some deviations from the isotropic estimate may be expected, although it is not possible to ascertain the effects of anisotropy on the energy flux with our available two-dimensional data.

In the dynamic model, the coefficients are calculated dynamically during the LES (which has a resolution of Δ) by filtering the simulated data at a scale $\alpha\Delta$, and determining C_s from

$$(C_S^{\Delta, DM})^2 = \langle L_{ij} M_{ij} \rangle / \langle M_{ij} M_{ij} \rangle, \tag{2.5}$$

$$L_{ij} = \overline{\tilde{\bar{u}}_i \tilde{\bar{u}}_j} - \tilde{\bar{u}}_i \tilde{\bar{u}}_j, \tag{2.6}$$

$$M_{ij} = -2\Delta^2(\alpha^2 |\tilde{\bar{S}}| \tilde{\bar{S}}_{ij} - \overline{|\tilde{S}| \tilde{S}_{ij}}), \tag{2.7}$$

where the overbar indicates spatial filtering at a scale $\alpha\Delta$ and L_{ij} is the so-called Leonard term.

A number of studies, e.g. Liu, Meneveau & Katz (1994), Chen, Katz & Meneveau (2005), have been carried out to evaluate the performance of SGS models based on two-dimensional PIV data. Following these studies, a two-dimensional top-hat filter is employed to spatially filter the velocity field. The spatial derivatives are obtained using the second-order finite differencing on a coarse grid of the filter size to mimic numerical evaluation in LES with grid-spacing of Δ. Since we do not have three-dimensional data to calculate all the required tensor components, the contractions are approximated by their two-dimensional surrogates, namely

$$\Pi^{\Delta}_{xy} = -(\tau_{11}\tilde{S}_{11} + \tau_{22}\tilde{S}_{22} + 2\tau_{12}\tilde{S}_{12}), \quad \Pi^{\Delta}_{xz} = -(\tau_{11}\tilde{S}_{11} + \tau_{33}\tilde{S}_{33} + 2\tau_{13}\tilde{S}_{13}), \tag{2.8}$$

$$|\tilde{S}_{2D,xy}|^2 = 2(\tilde{S}_{11}\tilde{S}_{11} + \tilde{S}_{22}\tilde{S}_{22} + 2\tilde{S}_{12}\tilde{S}_{12}), \quad |\tilde{S}_{2D,xz}|^2 = 2(\tilde{S}_{11}\tilde{S}_{11} + \tilde{S}_{33}\tilde{S}_{33} + 2\tilde{S}_{13}\tilde{S}_{13}). \tag{2.9}$$

All the variables introduced in (2.2)–(2.7) are calculated using the planar components. In the current analysis, the mean SGS energy fluxes and Smagorinsky coefficients are obtained based on ensemble-averaging of 5000 realizations and then spatial averaging along horizontal lines, which consist of 100 data points and span about 2λ. This process achieves better statistical convergence but eliminates the spatial variability occurring in the roughness sublayer.

Conditional sampling/averaging is implemented primarily in the current analysis to identify flow structures associated with significant SGS energy flux or high resolved strain rate. This approach has already been used extensively to obtain phase- or ensemble-averaged information associated with organized structures (Antonia 1981). To perform the sampling, the instantaneous realizations are scanned for regions satisfying a certain condition, e.g. an SGS energy flux exceeding a specified threshold. In x–y plane data, the scanning is performed only along a streamwise line located at a prescribed elevation, whereas in x–z planes the entire field of view is scanned. Subsequently, the points satisfying the condition along with the surrounding flow field are shifted to the same position, i.e. to (0, 0) in the x–z plane, and to (0, prescribed y) in the x–y plane. The results are then averaged to obtain the conditionally sampled flow field, denoted by $[\![\,]\!]$. The averaging procedure substantially increases the number of samples available for each prescribed condition, which greatly improves the statistical convergence of measured trends. Note that this procedure also uses unequal amounts of data in regions located at different distances from the point satisfying the prescribed condition, which is accounted for during the averaging. Comparisons of the statistics show that this averaging procedure yields trends that are similar to (but clearer than) those obtained from sampling at a fixed point. During the analysis, we compare the resulting flow structure to instantaneous realizations to determine to what extent the conditional averaging generates artifacts, as it does in some cases.

3. Results

3.1. *Mean SGS turbulence quantities*

In this section, the mean SGS turbulence quantities including production and dissipation rate for the x–y plane are obtained as defined in § 2.2.2. Figure 3 illustrates the mean SGS fluxes for $\Delta = k, 3k, 6k, \lambda$ and 2λ, along with mean shear production

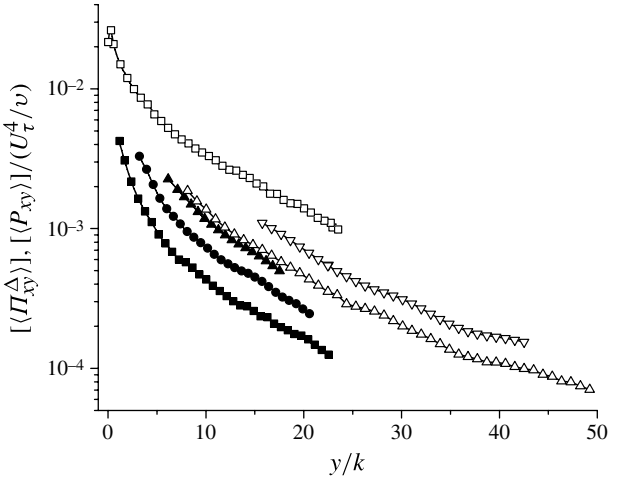

FIGURE 3. Mean two-dimensional surrogates of the SGS energy flux for filter scales of k (■), $3k$ (●), $6k$ (▲), λ (△) and 2λ (▽), along with the in-plane contributions to the spatially averaged TKE production rate (□).

rate calculated using

$$[\langle P_{xy} \rangle](y) = -\left[\langle u'v' \rangle \partial \langle u \rangle / \partial y\right], \tag{3.1}$$

where [ ] indicates spatial averaging over all points at the same elevation. This term represents most of the total TKE production rate, especially after spatial averaging. As noted before, unlike the results of $\Delta = k, 3k$ and $6k$, the SGS energy fluxes at $\Delta = \lambda$ and 2λ are calculated using the low-resolution dataset. We have also computed the flux for $\Delta = \lambda$ using both the original and sub-sampled (one of every 7 vectors) high-resolution data. Since the results agree well with those obtained using the low-resolution data filtered at the same scale, they are not shown. For the smallest filtering scales, the filtering contains 7×7 vectors. Larger scales involve more vectors. As shown in figure 3, all the mean SGS energy fluxes follow a similar trend to the production. Namely, they increase rapidly as the wall is approached. For the same elevation, the flux increases with increasing filter scale (note that the vertical axis is the logarithmic scale), and the differences increase as the wall is approached. This trend indicates an increasing contribution to the flux from eddies with sizes falling between the filter scales and the dissipation scale. As discussed later, almost all of the energy dissipation occurs at scales smaller than λ. However, very near the wall, turbulence production occurs over a broad range of scales due to the roughness-related spatial non-uniformities in the mean flow. As this effect diminishes away from the wall, the shear term becomes the primary contributor to the TKE production rate. Although scales smaller than Δ contribute to the TKE shear production rate, this contribution also diminishes with increasing y. For $\Delta = \lambda$ (for example) and $y \geqslant 2\lambda$, the contribution of subgrid scales to the mean production rate is negligible, as verified using the present data (not shown). Consequently, $[\langle \Pi^{\lambda} \rangle]$ should be close in magnitude to $[\langle P_{xy} \rangle]$. In figure 3, $[\langle \Pi^{\lambda} \rangle]/[\langle P_{xy} \rangle] \sim 0.5$ for $y \geqslant 2\lambda$, consistent with the expected $[\langle \Pi^{\lambda}_{xy} \rangle]/[\langle \Pi^{\lambda} \rangle] = 7/15$ for homogeneous isotropic turbulence (Van Hout *et al.* 2007), although the turbulence in this region is not fully isotropic.

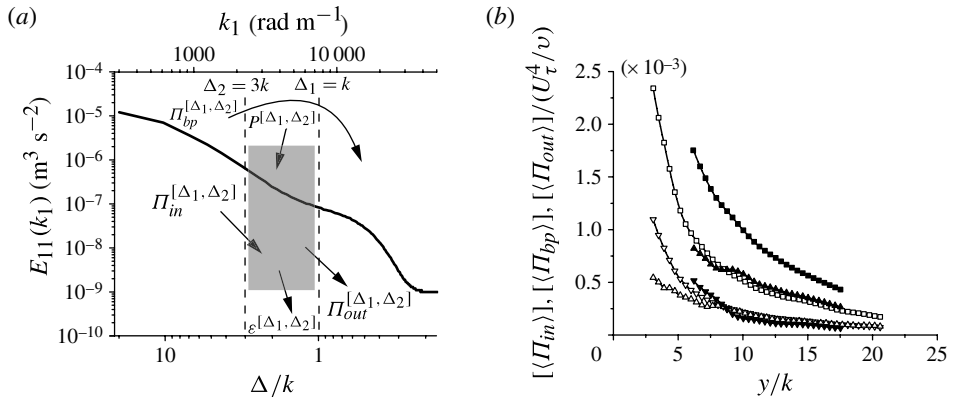

FIGURE 4. (*a*) A schematic showing turbulent energy fluxes into, out of and bypassing the scale range $[\Delta_1, \Delta_2]$, along with the production and dissipation rates in this scale range. The horizontal axis has two scales: the top axis is the wavenumber, k_1, and the bottom axis is Δ/k, which decreases with increasing wavenumber. In the present study, the two dashed vertical bars from left to right correspond to k, $3k$, respectively. (*b*) The measured x–y plane turbulent energy flux into (□), out of (△) and bypassing (▽) the scale range $[k, 3k]$, as well as flux into (■), out of (▲) and bypassing (▼) the scale range $[3k, 6k]$.

Considering two filters of size Δ_1 and Δ_2 ($\Delta_2 > \Delta_1$), the energy transfer, production and dissipation associated with scale range $[\Delta_1, \Delta_2]$ are illustrated in figure 4(*a*). The energy flux across Δ_2, i.e. Π^{Δ_2}, can be decomposed into two components:

$$\Pi_{in}^{[\Delta_1,\Delta_2]} = -L_{ij}\tilde{\bar{S}}_{ij}, \tag{3.2}$$

$$\Pi_{bp}^{[\Delta_1,\Delta_2]} = -\bar{\tau}_{ij}\tilde{\bar{S}}_{ij}, \tag{3.3}$$

where $\sim$ and the overbar represent filtering at Δ_1 and Δ_2, respectively (Δ_2 is equivalent to $\alpha\Delta_1$ in (2.5)–(2.7)). Following Liu *et al.* (1994), L_{ij} is the stress associated with motions with scales falling between Δ_1 and Δ_2. Accordingly, $\Pi_{in}^{[\Delta_1,\Delta_2]}$ is termed the 'local' energy flux from turbulence at scales larger than Δ_2 to the $[\Delta_1, \Delta_2]$ range. Since $\Pi_{bp}^{[\Delta_1,\Delta_2]}$ is equal to the difference between Π^{Δ_2} and $\Pi_{in}^{[\Delta_1,\Delta_2]}$, it represents the energy transfer from turbulence with scales larger than Δ_2 to those that are smaller than Δ_1. Thus, it is referred to as 'not-so-local' flux in Liu *et al.* (1994) or 'non-local' flux in the present paper. In the same spirit, $\Pi_{out}^{[\Delta_1,\Delta_2]}$, which is the energy cascading down from the $[\Delta_1, \Delta_2]$ to adjacent smaller scales, is also a 'local' energy flux. It is calculated using

$$\Pi_{out}^{[\Delta_1,\Delta_2]} = \Pi^{\Delta_1} - \Pi_{bp}^{[\Delta_1,\Delta_2]} \tag{3.4}$$

(see sketch in figure 4*a*). For the $[\Delta_1, \Delta_2]$ range, the balance of energy flux terms is

$$\Pi_{in}^{[\Delta_1,\Delta_2]} + P^{[\Delta_1,\Delta_2]} = \Pi_{out}^{[\Delta_1,\Delta_2]} + \varepsilon^{[\Delta_1,\Delta_2]}, \tag{3.5}$$

where $P^{[\Delta_1,\Delta_2]}$ accounts for the energy production due to mean flow strain in the $[\Delta_1, \Delta_2]$ range, and $\varepsilon^{[\Delta_1,\Delta_2]}$ is the local energy dissipation within $[\Delta_1, \Delta_2]$. This expression follows from the energy balance if one neglects spatial fluxes and assumes statistically steady flow. Moreover, for our targeted scale ranges $[k, 3k]$, $[3k, 6k]$ and $[\lambda, 2\lambda]$, we assume that the local energy production is negligible compared with

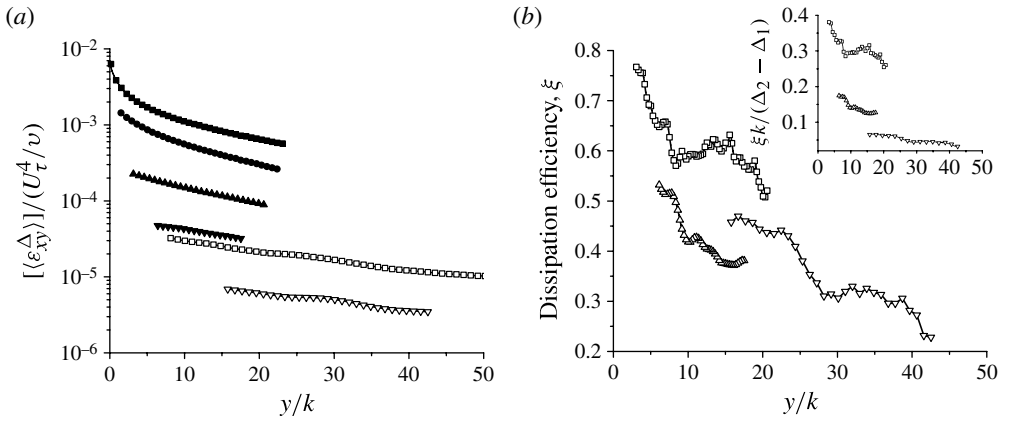

FIGURE 5. (*a*) In-plane contributions to dissipation rate calculated using the non-filtered velocity field (■), and tophat-filtered velocity at length scale of k (●), $3k$ (▲), $6k$ (▼), λ (□), and 2λ (▽). (*b*) Dissipation efficiency within scale ranges $[k, 3k]$ (□), $[3k, 6k]$ (△) and $[\lambda, 2\lambda]$ (▽). The insert shows the dissipation efficiency re-scaled by the span of each scale range.

dissipation. Therefore, the difference between energy fluxes into and out of these scale ranges is assumed to be equal to the amount of energy being dissipated by molecular viscosity within that range. Accordingly, we introduce dissipation efficiency

$$\xi = ([\langle\Pi_{in}^{[\Delta_1,\Delta_2]}\rangle] - [\langle\Pi_{out}^{[\Delta_1,\Delta_2]}\rangle])/[\langle\Pi_{in}^{[\Delta_1,\Delta_2]}\rangle], \tag{3.6}$$

which quantifies how dissipative the turbulence in the $[\Delta_1, \Delta_2]$ range is. As an illustration, figure 4(*b*) shows mean energy fluxes into, out of and bypassing the $[k, 3k]$ and $[3k, 6k]$ ranges. Trends of fluxes associated with the two ranges are substantially different for $y > \Delta_2$, i.e. at elevations where the Leonard term does not disappear. Specifically, $[\langle\Pi_{bp}^{[k,3k]}\rangle]$ grows significantly faster than $[\langle\Pi_{out}^{[k,3k]}\rangle]$ with decreasing distance from the wall, but they converge in the outer layer. This trend indicates that the 'non-local' flux is the dominant contributor to the near-wall increase of $[\langle\Pi_{xy}^{k}\rangle]$ ($\Pi_{xy}^{k} = \Pi_{bp}^{[k,3k]} + \Pi_{out}^{[k,3k]}$) shown in figure 3. Conversely, $[\langle\Pi_{bp}^{[3k,6k]}\rangle]$ is significantly smaller than $[\langle\Pi_{out}^{[3k,6k]}\rangle]$ over all the present elevations, indicating that the typical cascading process of turbulence is prominent for this range. Note that when the energy fluxes are scaled with the local production rate (results not shown), both $[\langle\Pi_{out}^{[k,3k]}\rangle]/[\langle P_{xy}\rangle]$ and $[\langle\Pi_{out}^{[3k,6k]}\rangle]/[\langle P_{xy}\rangle]$ remain almost constant with varying elevations, while the scaled non-local fluxes still increase near the wall. These observations are a statistical manifestation of two key phenomena. First, in the roughness sublayer, the interaction of large-scale flow structures with the roughness itself enhances the direct energy transfer from large to small scales, bypassing the typical cascading process. Presumably, this interaction bears a resemblance to phenomena occurring in canopy turbulent flows discussed by Finnigan (2000). He proposed an energy bypass scheme in which the aerodynamic drag on the foliage causes a 'spectral short cut', which moves energy directly from large to fine scales. Second, when the filter scale falls above that of the roughness-scale eddies, the non-local effects diminish relative to the local ones, demonstrating the significant role of these eddies in the turbulence dissipation.

In order to further illustrate the impact of the roughness-scale eddies, figure 5(*a*) shows the mean 'two-dimensional dissipation' calculated based on the in-plane

velocity gradient (Doron *et al.* 2001) of the filtered velocity fields

$$[\langle \varepsilon_{xy}^{\Delta} \rangle](y) = \upsilon \left[3 \left\langle \left(\frac{\partial \tilde{u}'}{\partial x} \right)^2 \right\rangle + \left\langle \left(\frac{\partial \tilde{u}'}{\partial y} \right)^2 \right\rangle + \left\langle \left(\frac{\partial \tilde{v}'}{\partial x} \right)^2 \right\rangle + 3 \left\langle \left(\frac{\partial \tilde{v}'}{\partial y} \right)^2 \right\rangle + 2 \left\langle \frac{\partial \tilde{u}'}{\partial x} \frac{\partial \tilde{v}'}{\partial y} \right\rangle + 2 \left\langle \frac{\partial \tilde{u}'}{\partial y} \frac{\partial \tilde{v}'}{\partial x} \right\rangle \right]. \tag{3.7}$$

In fully resolved isotropic turbulence, this expression would represent 8/15 of the total dissipation rate. Since filtering reduces the spatial resolution and thus the magnitude of spatial derivatives, $\varepsilon_{xy}^{\Delta}$ is an estimate of the contribution of scales larger than that of the filter size to the total molecular dissipation rate. As expected, figure 5(*a*) shows that the mean molecular dissipation rate of the filtered field decreases significantly with increasing filter size. Filtering the data with $\Delta = k$ causes a ∼50 % drop. When $\Delta > 3k$, $[\langle \varepsilon_{xy}^{\Delta} \rangle]$ is attenuated to less than 5 % of the value for the unfiltered field. Note also that dissipation rates calculated from two different datasets, with close filter size, i.e. $6k$ and λ, display consistent trend and magnitude. The dissipation efficiency plot (figure 5*b*) shows that the turbulence in the $[k, 3k]$ range is substantially more dissipative than that in the $[3k, 6k]$ range. Both efficiency curves rise rapidly near the wall, where the roughness-scale eddies dissipate more than 70 % of the energy influx. Notably, the dissipative efficiency of these eddies remains more than 50 % even well above the roughness sublayer, reaffirming the excess impact of roughness eddies in the outer layer. Since (3.6) does not account for the difference in the range of scales involved, the dissipation efficiency at large scales ($[\lambda, 2\lambda]$) appears higher than that in the $[3k, 6k]$ range. To take this difference into account, dissipation efficiency multiplied by $k/(\Delta_2 - \Delta_1)$ is plotted as an insert in figure 5(*b*). It indicates that this pre-multiplied dissipation efficiency increases with deceasing filter size, as expected, with substantially higher values in the $[k, 3k]$ range.

The measured SGS dissipation-based Smagorinsky coefficients are compared with those obtained from the standard dynamic model in figure 6. The coefficients are presented with the horizontal axis scaled by the corresponding filter size. For the dynamic model, the filter size is taken to be $\alpha\Delta$. As a result of this scaling, most of the coefficients converge to values that increase at $y/\Delta < 2$, and then plateau in a band of 0.20–0.24, which is higher than the isotropic turbulence value of 0.16. In general, the dynamic model coefficients are about 10 % higher than the static values. The presently measured rise and plateau in coefficients is consistent with trends of scale-dependent dynamic coefficients in LES of high Reynolds number boundary layer flows by Porté-Agel, Meneveau & Parlange (2000). However, their coefficients increase from 0.02 very near the wall to ∼0.13 in the outer layer. The reason for our elevated values of C_s might be associated with using only x–y plane data to calculate the coefficients. When we re-calculate C_s using x–z plane data (not shown since we do not have the y-dependence available from these data), the coefficients at $y = 11k$ fall in the 0.08–0.14 range, closer to values obtained in Porté-Agel *et al.* (2000). The discrepancy between the x–y and x–z plane results is caused by the differences in the contributions of the shear terms, e.g. $\langle \tau_{13} \tilde{S}_{13} \rangle$ is only about 40 % of $\langle \tau_{12} \tilde{S}_{12} \rangle$ at $y = 11k$.

3.2. *Conditionally averaged flow structure based on SGS energy flux*

In this section, conditional averaging is applied to study the flow structures associated with strong SGS energy transfer from large scales to roughness scales. Our primary interest is in the role of roughness-scale eddies. As a result, most of the conditional

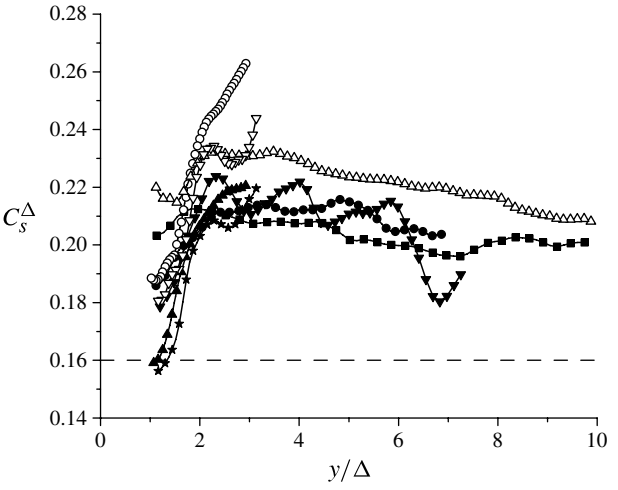

FIGURE 6. Measured Smagorinsky model coefficients for filter scales of k (■), $3k$ (●), $6k$ (▲), λ (▼), and 2λ (★), along with standard dynamic model coefficients for filter scale pairs of $[k, 2k]$ (△), $[3k, 6k]$ (○) and $[\lambda, 2\lambda]$ (▽). The solid horizontal line, $C_s^\Delta = 0.16$, corresponds to the static Smagorinsky coefficient for homogeneous, isotropic turbulence.

analysis is based on a filter scale of $3k$, unless stated otherwise. The procedures are described in § 2.2.2, and a sampling threshold is selected to include events with the highest 5 % of the SGS energy flux calculated using the two-dimensional surrogates at corresponding planes (equation (2.8)). As shown by Natrajan & Christensen (2006), these x–y plane two-dimensional surrogates approximate the true flux very well in events associated with strong SGS energy flux. Before discussing the conditionally averaged phenomena, figure 7 presents a sample instantaneous x–y plane realization to demonstrate typical flow structures associated with strong SGS energy flux before and after spatial filtering. A large inclined layer containing several clusters of predominantly negative vorticity is clearly visible across the entire plane ($\sim 6\lambda$) of the unfiltered flow (figure 7*a*). The space below this inclined layer is filled with roughness-scale vortices of both signs, including many powerful positive ones. Above the layer, the vorticity magnitude decreases abruptly. In the corresponding $3k$-filtered flow (figure 7*b*), the vortex clusters within the inclined layer are replaced by a series of discrete vortices that are separated by $\sim\lambda$. This pattern clearly shows that the surface signature persists outside the roughness sublayer. The contours of Π_{xy}^{3k} indicate that the SGS flux maxima develop within the layer, between the vortices. A very similar pattern of vortices with SGS flux peaks between them has been observed in the outer part of smooth-wall boundary layers by Natrajan & Christensen (2006). This pattern was attributed to the signature of hairpin packets in their study. The most probable mechanisms that generate this structure near the rough wall in the present study are discussed in § 3.3.

Figure 8 shows the conditionally averaged velocity vector field for a conditioning point located at $y = 11k$, as marked with a solid dot at $(0, 11k)$. This plot does not extend to the wall since the lowest filtered flow elevation is constrained by the filter size. Clearly, a large-scale inclined shear layer extends across the entire field of view of 5λ in the streamwise direction. A strong ejection ($u' < 0, v' > 0$) occurs downstream and below the conditioning point, and a weaker sweep ($u' > 0, v' < 0$)

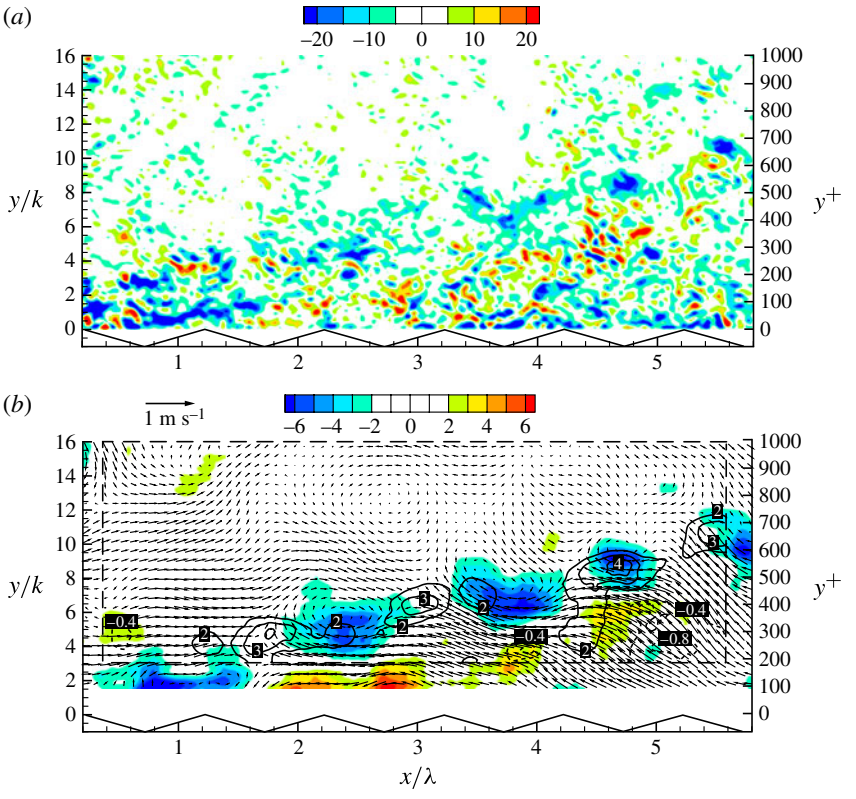

FIGURE 7. An instantaneous sample of (*a*) the original, (*b*) the corresponding 3*k*-filtered velocity vectors and colour floods of spanwise vorticity along with black contour lines of $\Pi_{xy}^{3k}h/U_\tau^2U_c$ (available only in the region marked by the dashed box). For clarity, only one in four vectors is plotted, in both directions.

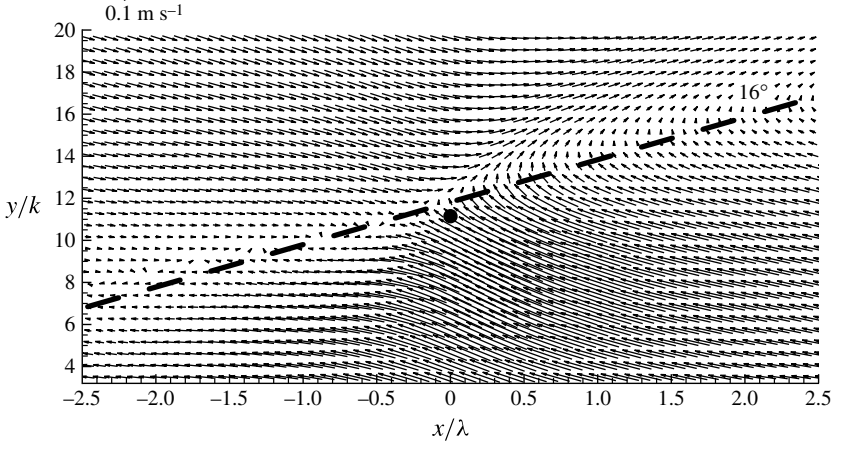

FIGURE 8. Conditionally averaged filtered vector map for the highest 5 % of Π_{xy}^{3k} at $y = 11k$. The point where the condition is satisfied is shifted horizontally to $x/\lambda = 0$ (marked by a solid dot). For clarity, only one in four vectors is plotted, in both directions. The inclined dashed line marks the shear layer.

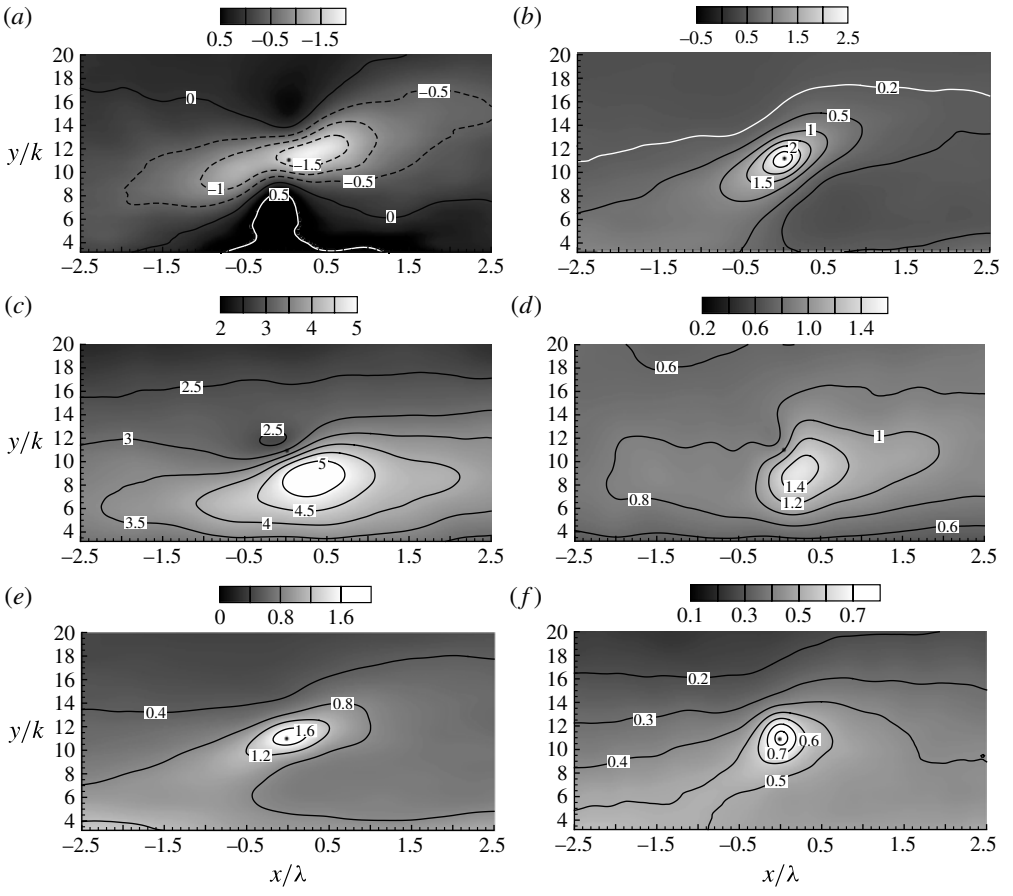

FIGURE 9. Distributions of (conditionally averaged) (*a*) $[\![\tilde{\omega}_z^{3k}]\!]h/U_c$, (*b*) $[\![\Pi_{xy}^{3k}]\!]h/U_\tau^2U_c$, (*c*) $[\![\widetilde{u'}^{3k}\widetilde{u'}^{3k}]\!]/U_\tau^2$, (*d*) $[\![\widetilde{v'}^{3k}\widetilde{v'}^{3k}]\!]/U_\tau^2$, (*e*) $[\![\tau_{11}^{3k}]\!]/U_\tau^2$ and (*f*) $[\![\tau_{22}^{3k}]\!]/U_\tau^2$ for the highest 5 % of Π_{xy}^{3k} at $y = 11k$.

covers the area upstream and above it. The corresponding vorticity field (figure 9*a*) shows an inclined layer of negative vorticity bounded by substantially weaker positive vorticity below and above. Within this layer, the negative vorticity peaks slightly downstream of the sampling point. This trend is consistent with the typical position of regions with high strain rate between vortices, and consequently the fact that SGS energy flux peaks between vortices in instantaneous realizations (figure 7*b*). The corresponding distribution of SGS energy flux $[\![\Pi_{xy}^{3k}]\!]$ (figure 9*b*) peaks at $(0, 11k)$, by construction. A region of elevated SGS flux extends behind this point at a higher inclination angle compared with that of the vorticity. The flux is low downstream and below as well as upstream and above the conditioning point, but remains relatively high at low elevations upstream of the peak. As will be discussed later, this pattern is associated with the entrainment of near-wall flow structures from the roughness sublayer. Figures 9(*c*) and 9(*d*) show the corresponding resolved TKE components, i.e. $[\![\widetilde{u'}^{3k}\widetilde{u'}^{3k}]\!]$ and $[\![\widetilde{v'}^{3k}\widetilde{v'}^{3k}]\!]$, respectively. Their distributions vary, but the maxima of both components are located downstream and below the SGS flux peak, well within

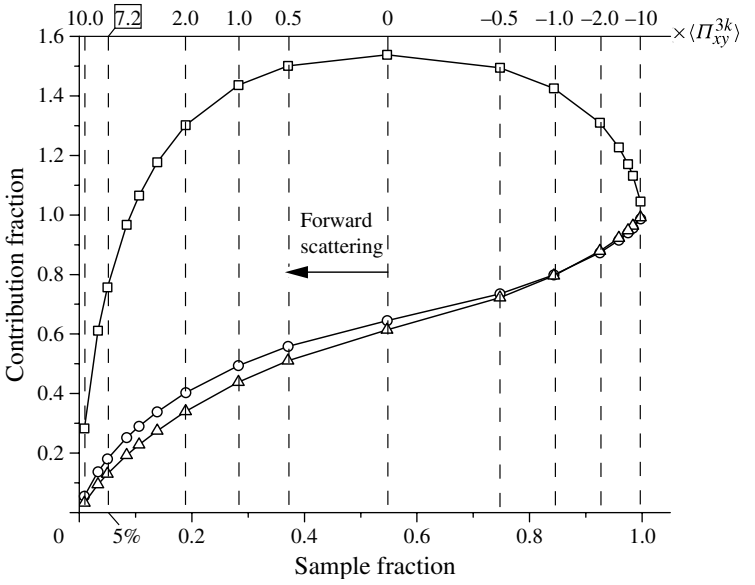

FIGURE 10. Sample fraction (bottom horizontal axis) and relative contribution (vertical axis) of the data to the average values of SGS energy flux (□, $\langle\Pi_{xy}^{3k}\rangle$) and SGS kinetic energy components (○, $\langle\tau_{11}^{3k}\rangle$; △, $\langle\tau_{22}^{3k}\rangle$). The top axis displays the corresponding threshold value in units of the mean SGS energy flux.

the ejection region (figure 8). They also have minima centred upstream and above the conditioning point. The resolved in-plane TKE, $1/2[\![\widetilde{u}_i'^{3k}\widetilde{u}_i'^{3k}]\!]$ (not shown), has a similar pattern to the dominant contributor $[\![\widetilde{u}'^{3k}\widetilde{u}'^{3k}]\!]$. The corresponding distributions of normal SGS stress components, $[\![\tau_{11}^{3k}]\!]$ and $[\![\tau_{22}^{3k}]\!]$, are presented in figures 9(*e*) and 9(*f*). Their spatial distributions are similar to that of the SGS energy flux, peaking right at the conditioning point. Clearly, the SGS kinetic energy does not achieve a maximum at the same location as that of the resolved TKE. However, one should keep in mind that these observations do not represent a contradiction to similarity-based or dynamic SGS stress models (Liu *et al.* 1994; Meneveau & Katz 2000), which are based on the smallest of the resolved scales. In fact, using a filter with size 2Δ and calculating the modelled stresses (not shown) gives spatial distributions that are consistent with those of figures 9(*e*) and 9(*f*). The structures causing the shift in the location of the resolved TKE are much larger than the filter scale.

Although the conditionally averaged flow structure and distribution of stresses depend quantitatively on the threshold level, the general flow pattern remains consistent. Insensitivity of flow structure involved with high SGS flux to the threshold level is also reported by Piomelli *et al.* (1996) and Natrajan & Christensen (2006) for smooth-wall boundary layers. Figure 10 compares the fraction of points at elevation $y = 11k$ in which Π_{xy}^{3k} exceeds a certain threshold level to the contribution of these points to the overall flux. Threshold levels corresponding to a number of fractions have a nonlinear distribution, as indicated at the top horizontal axis. Evidently, Π_{xy}^{3k} is positive in 54 % of the points and the average positive contribution (including only positive contributions) is 154 % of the average flux. It is remarkable that a small fraction of the flow field with high Π_{xy}^{3k} generates most of energy flux from

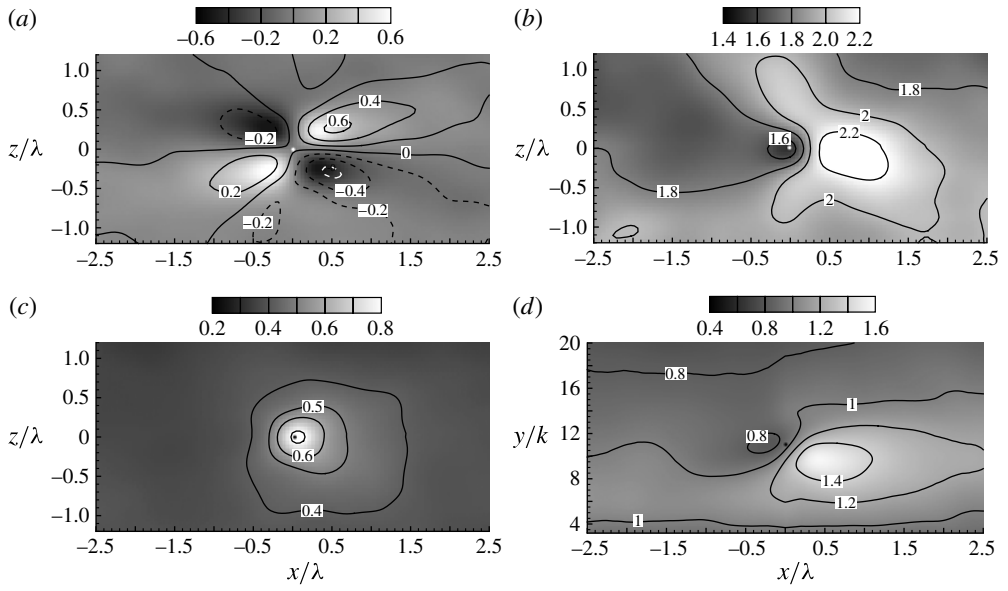

FIGURE 11. Distributions (x–z plane) of (a) $[\![\tilde{\omega}_y^{3k}]\!]h/U_c$, ($b$) $1/2[\![\widetilde{u_i'}^{3k}\widetilde{u_i'}^{3k}]\!]/U_\tau^2$ and (c) $1/2[\![\tau_{ii}^{3k}]\!]/U_\tau^2$ for the highest 5 % of $-\tau_{11}^{3k}\tilde{S}_{11}^{3k}$ at $y = 11k$. Distributions (x–y plane) of (d) $1/2[\![\widetilde{u_i'}^{3k}\widetilde{u_i'}^{3k}]\!]/U_\tau^2$ for the highest 5 % of $-\tau_{11}^{3k}\tilde{S}_{11}^{3k}$ at $y = 11k$.

resolved to subgrid scales (positive flux). For example, 5 % of the data with the highest flux, corresponding to a threshold of $\Pi_{xy}^{3k} > 7.2\langle\Pi_{xy}^{3k}\rangle$ (the condition used in figures 8 and 9), contributes about 50 % of the positive flux. Similarly, 9 % of the points contribute 67 %, and 18 % of the points contribute 84 % of the positive flux. The same trend applies to $\Pi_{xy}^{3k} < 0$, i.e. a small fraction of the flow field, where the backscatter of energy is large, generates most of the negative flux. These trends agree with DNS results reported by Piomelli *et al.* (1996) for smooth-wall boundary layers at low Reynolds numbers. In contrast, except for extreme (positive or negative) energy flux events, the contributions to SGS kinetic energy components, also presented in figure 10, are not significantly different from the corresponding fraction of realizations. For example, points satisfying the above-mentioned highest 5 % flux condition contribute ∼15 % of the total SGS kinetic energy. A general conclusion of these observations is that an overwhelming majority of SGS energy flux is caused by a small fraction of flow structures. However, SGS kinetic energy and stresses are much more broadly distributed.

To obtain an x–z plane view of the structure that generates the large SGS energy flux, we repeat the conditional sampling using x–z plane data at the same elevation ($y = 11k$) based on high $-\tau_{11}^{3k}\tilde{S}_{11}^{3k}$, which is the only common term between Π_{xy}^{3k} and Π_{xz}^{3k}. Two pairs of counter-rotating vortices with an in-pair spacing of ∼0.5λ appear in the wall-normal vorticity distribution (figure 11*a*). The pair located downstream of the sampling point creates a region with backflow between the vortices, whereas the pair located upstream induces a forward flow between the vortices. Consequently, the sampling point is subjected to strong streamwise (resolved-scale) contraction, which

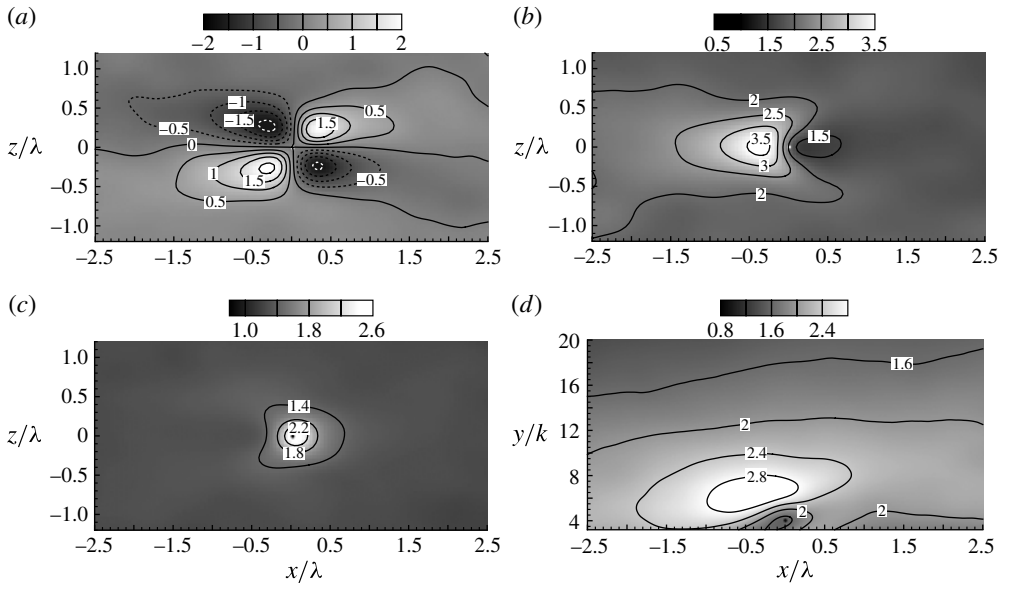

FIGURE 12. Distributions (x–z plane) of (*a*) $[\![\tilde{\omega}_y^{3k}]\!]h/U_c$, (*b*) $1/2[\![\widetilde{u_i'}^{3k}\widetilde{u_i'}^{3k}]\!]/U_\tau^2$ and (*c*) $1/2[\![\tau_{ii}^{3k}]\!]/U_\tau^2$ for the highest 5 % of Π_{xz}^{3k} at $y = 1k$. Distributions (x–y plane) of (*d*) $1/2[\![\widetilde{u_i'}^{3k}\widetilde{u_i'}^{3k}]\!]/U_\tau^2$ for the highest 5 % of Π_{xy}^{3k} at $y = 4.2k$.

causes the maxima of SGS kinetic energy (figure 11*c*) and flux at this location, along with spanwise expansion. These patterns are consistent with and complement the observed ejection-sweep structure in the x–y plane (figure 8). Slicing the inclined shear layer with a horizontal plane would position the ejection region downstream of the conditioning point and the sweep region upstream of it. At $y = 11k$, the downstream pair has higher magnitude of vorticity and induces stronger backflow than the upstream pair. Accordingly, the resolved TKE (figure 11*b*) peaks downstream of the sampling points. The peak location coincides with that of ejection in the corresponding x–y plane results obtained by applying the same condition (figure 11*d*). The observed flow structure raises the question of the effect of streamwise contraction on the SGS energy flux in our conditionally averaged results. Although the shear term plays a major role, the contribution of streamwise contraction is substantial. Based on the x–y plane data, $-[\![\tau_{11}^{3k}\tilde{S}_{11}^{3k}]\!]$ contributes 38 % of $[\![\Pi_{xy}^{3k}]\!]$, comparable to the 44 % contributed by the shear term at the sampling point. In the x–z plane 42 % of $[\![\Pi_{xz}^{3k}]\!]$ comes from the $-[\![\tau_{11}^{3k}\tilde{S}_{11}^{3k}]\!]$ term at $y = 11k$.

Elevation effects on the conditionally averaged flow structure generating high SGS flux events are examined by repeating the analysis using sampling points or planes located closer to the wall. The x–z plane data analysis (figure 12*a*–*c*) is performed within the roughness sublayer, at $y = k$. Here the highest 5 % condition is applied only based on Π_{xz}^{3k}, but $\tau_{11}^{3k}\tilde{S}_{11}^{3k}$-based analysis shows similar patterns. The conditionally averaged, resolved vorticity distribution (figure 12*a*) exhibits two pairs of counter-rotating vortices, which is qualitatively similar to that in the outer layer (figure 11*a*). However, at this elevation, the upstream pair is stronger than the downstream one, and accordingly, the resolved TKE (figure 12*b*) peaks upstream of the sampling

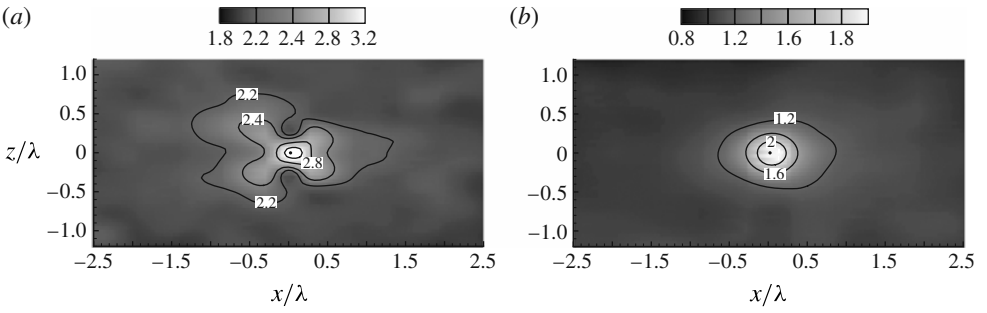

FIGURE 13. Distributions of $[\![|\tilde{\omega}_y^{3k}|]\!]h/U_c$ at (*a*) $y = 1k$ and (*b*) $y = 11k$ for the highest 5 % of Π_{xz}^{3k}.

point. Constrained by the filter size, we cannot perform the conditional averaging at $y = k$ in the x–y plane. Instead, the averaging is performed at $y = 4.2k$, a little higher than the lowest elevation where the filtered strain rate is available for $\Delta = 3k$. Figure 12(*d*) shows the x–y plane distribution of resolved kinetic energy, sampled based on a threshold for Π_{xy}^{3k}. As is evident, the resolved TKE peak shifts to the sweeping region above and upstream of the conditioning point, consistent with the x–z plane results (figure 12*b*). In agreement with the present trends, Hong *et al.* (2011) show that sweeping motions are the primary contributors to momentum flux (Reynolds shear stress) in the roughness sublayer, whereas ejections are dominant in the outer layer. Except for the displacement associated with conditioning location, the x–y plane distributions of spanwise vorticity, SGS kinetic energy and flux (not shown) are similar to results in the outer layer (figure 8). They indicate that the mismatch between the location of resolved and SGS kinetic energy maxima persists near the wall, with the latter peaking at the conditioning point (figure 12*c*). In both planes, the anisotropy in (instantaneous) SGS stresses peaks at the conditioning point (not shown), suggesting that energy transfer and anisotropy are coupled. Both of them also decay with increasing distance from the wall. For example, for points satisfying the high SGS energy flux condition, $|[\![\tau_{11}^{3k}/\tau_{33}^{3k}]\!]| = 2.6$ at $y = 1k$ and 1.1 at $y = 11k$. Also, $|[\![\tau_{11}^{3k}/\tau_{22}^{3k}]\!]| = 4.1$ at $y = 4.2k$ and 1.9 at $y = 11k$.

In contrast to the similarity in vorticity distributions (figures 11*a* and 12*a*), the distributions of the vorticity magnitude reveal significantly different features. Near the wall, the region of high vorticity magnitude has a cross pattern (figure 13*a*), suggesting (although not proving) the co-occurrence of two counter-rotating vortex pairs (figure 12*a*). Conversely, in the outer layer, the cross pattern disappears and is replaced by an oval peak centred at the sampling point (figure 13*b*). This distribution implies that the two vortex pairs do not always appear at the same time, and that the pattern in figure 11(*a*) is likely an artifact of averaging. The justification of this statement is provided by examining instantaneous realizations in § 3.3.

The effect of the filter scale on the flow structure is investigated by comparing the statistics for $\Delta = \lambda$ to those obtained for $\Delta = 3k$ at the same elevation ($y = 11k$) and SGS energy flux threshold (the highest 5 %). The Π_{xy}^{λ}-based analysis is performed using the low-resolution x–y plane data (see table 1), and representative results are provided in figure 14(*a*,*b*). The long inclined negative-vorticity layer bounded by positive regions on both sides is evident in figure 14(*a*), in agreement with the results obtained for a smaller filter. However, the negative vorticity peaks within the layer are

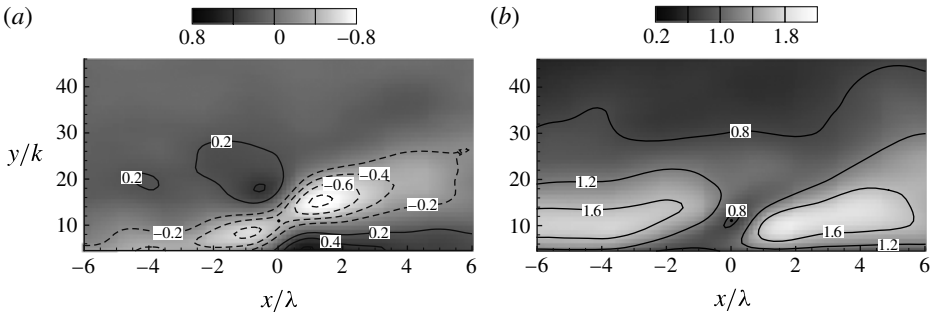

FIGURE 14. Distributions of (*a*) $[\![\tilde{\omega}_z^{\lambda}]\!]h/U_c$ and (*b*) $1/2[\![\widetilde{u_i'}^{\lambda}\widetilde{u_i'}^{\lambda}]\!]/U_\tau^2$ for the highest 5 % of Π_{xy}^{λ} at $y = 11k$.

pushed farther away, to a distance of approximately one filter size from the sampling point. Similar to the results for $\Delta = 3k$, the resolved TKE (figure 14*b*) is also minimal at the peak of SGS kinetic energy, but its magnitude is balanced in the sweep and ejection regions, unlike the ejection dominance observed with the smaller filter. This discrepancy could be explained by the tendency of the sweep upstream to carry more large-scale energy compared to the ejection downstream. Consequently, increasing the filter size retains relatively more resolved TKE in the sweep region.

3.3. *Flow structures associated with strong SGS energy flux*

3.3.1. *Observations on instantaneous realizations*

In this section, we examine instantaneous realizations in order to clarify their differences and similarities with flow structures revealed by conditionally averaged results. An instantaneous sample of the original and filtered flow field at the x–y plane involved with high Π_{xy}^{3k} has already been presented in figure 7. Figure 15 shows an x–z plane view of a typical instantaneous flow pattern with high Π_{xz}^{3k} at $y = k$. The unfiltered wall-normal vorticity field (figure 15*a*) is filled with roughness-scale (i.e. scale of k) eddies with opposite signs. When a $3k$ filter is applied to this vorticity map (figure 15*b*), it reveals two trains of counter-rotating vortices that intersect each other. The spacing between adjacent vortices in each train is about λ. The distribution of Π_{xz}^{3k}, marked by black contour lines, peaks at the intersection of the vortex trains. The neighbouring vorticity resembles the pattern of the two counter-rotating vortex pairs observed in the conditional average (figure 12*a*). Although the instantaneous flow fields vary substantially, the peaking of SGS flux at the intersection of vortex trains is a persistent phenomenon at this elevation. Another instantaneous sample of filtered vorticity (figure 15*c*) provides clearer evidence for the existence of large-scale structures. As shown in the figure, two trains of counter-rotating vortices extend across the entire field of view, i.e. $\sim 6\lambda$ in the streamwise direction. These trains are nearly parallel, with $\sim \lambda/2$ spacing between them upstream and downstream of their intersection, where Π_{xz}^{3k} peaks.

Conversely, in the outer layer (at $y = 11k$), the intersecting pairs of counter-rotating vortex trains are rare, as demonstrated by a typical instantaneous sample of filtered vorticity (figure 15*d*). Instead, Π_{xz}^{3k} peaks inside the vortex train, with much lower magnitude than that near the wall. This representative sample suggests that the co-presence of two vortex pairs in the outer layer (figure 11*a*) is an artifact of the averaging procedure. Accordingly, the conditionally averaged distribution of vorticity

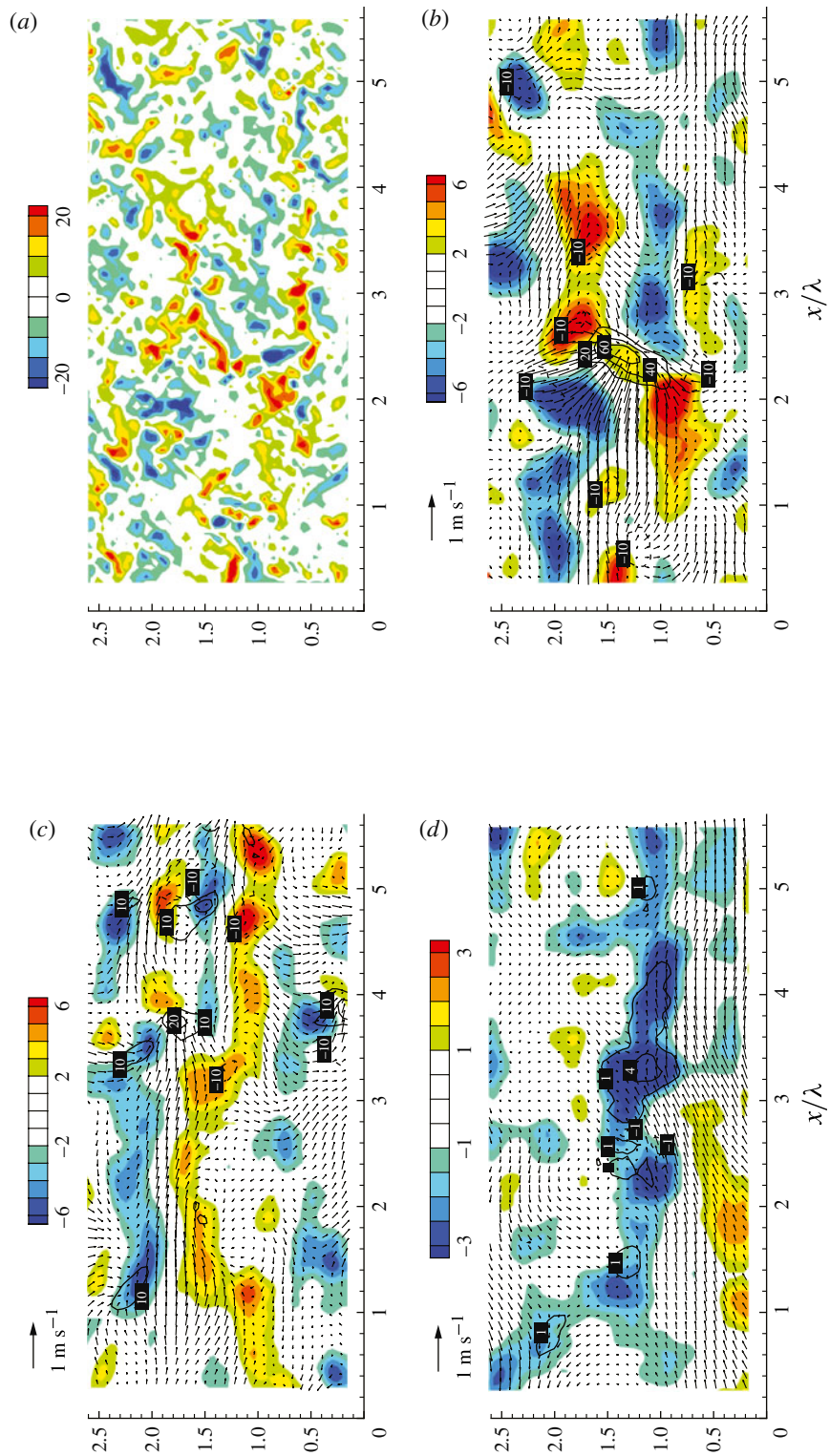

FIGURE 15. (*a*) Original and (*b*) corresponding 3*k*-filtered instantaneous sample of velocity fluctuations, colour floods of wall-normal vorticity $\tilde{\omega}_y^{3k}h/U_c$, and black contour lines of $\Pi_{xz}^{3k}h/U_\tau^2U_c$ at $y = 1k$. (*c*) Another sample of filtered flow at $y = 1k$. (*d*) An instantaneous sample of filtered flow at $y = 11k$. For clarity, only one in two vectors is plotted, in both directions.

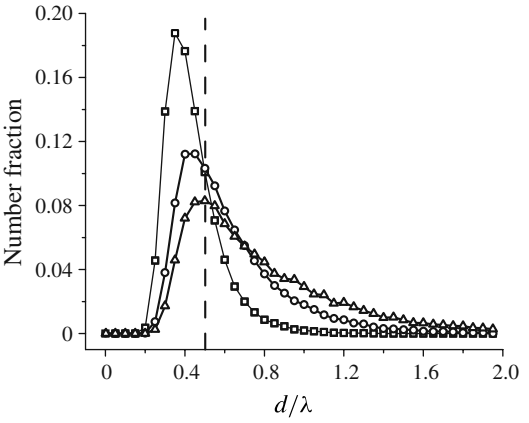

FIGURE 16. The p.d.f. of the minimum distance between two counter-rotating wall-normal vortices in x–z plane located at $y = 1k$ (□), $y = 5.5k$ (○) and $y = 11k$ (△).

magnitude (figure 13*b*) does not have a cross pattern at $y = 11k$. Nevertheless, the λ spacing between vortices within a single train, as a roughness signature, is evident both in the x–y plane (figure 7) and x–z plane views (figure 15*d*) of instantaneous samples.

To further illustrate the persistence of roughness signature, we calculate the probability density function (p.d.f.) of minimum distance between vortices of opposite signs at different x–z planes. To eliminate the effect of filter size, these vortices are identified based on the unfiltered swirling strength. Vortices with strength of less than 10 % of the averaged value and size of less than k ($\sim 0.15\lambda$) are not accounted for, in order to reduce the uncertainty. The results are summarized in figure 16. At $y = k$, the p.d.f. has a peak at 0.35λ, slightly lower than the spacing between two trains, which varies between 0.5λ and λ in the instantaneous sample (figure 15*b*). With increasing elevation, the p.d.f. broadens. At $y = 11k$, although counter-rotating vortex trains are rarely observed, at least within our field of view ($\sim 3\lambda$ in the spanwise direction), the most probable vortex spacing is still $\sim 0.5\lambda$. This signature coincides with the nearest spanwise spacing between roughness elements, and is not related to the distance from the wall, which is substantially larger than λ at this elevation. Like the spectral bumps shown in figure 1, this preferred 0.5λ spacing well above the roughness sublayer is another clear indication of the persistence of roughness signature.

The time-resolved PIV measurements provide us with the ability to observe the evolution of turbulent structures near the wall. Figure 17(*a*) is an x–z plane sample snapshot of the distribution of $\widetilde{u'}^{3k}$ at $y = k$, showing a broad sweep impinging on the rough surface. The high Π_{xz}^{3k} is produced due to the contraction at the interface between the sweep and a narrow ejection region within the sweeping zone. This pattern is strikingly similar to the corresponding conditionally averaged result (figure 12*b*), indicating that the conditional averaging does capture the characteristic features of the turbulent structure near the roughness. Figure 17(*b*) illustrates a process involving abrupt lifting of near-wall vortices within an area surrounded by a sweeping flow. The dashed red line marks the trajectory of a vortex, which rises from $y \sim 3k$ to $\sim 8k$ over a streamwise span of 3λ under the influence of a local ejection that develops below the sweep. These features agree with the near-wall conditionally averaged results (figure 12*d*), where the resolved TKE peaks in a sweeping region

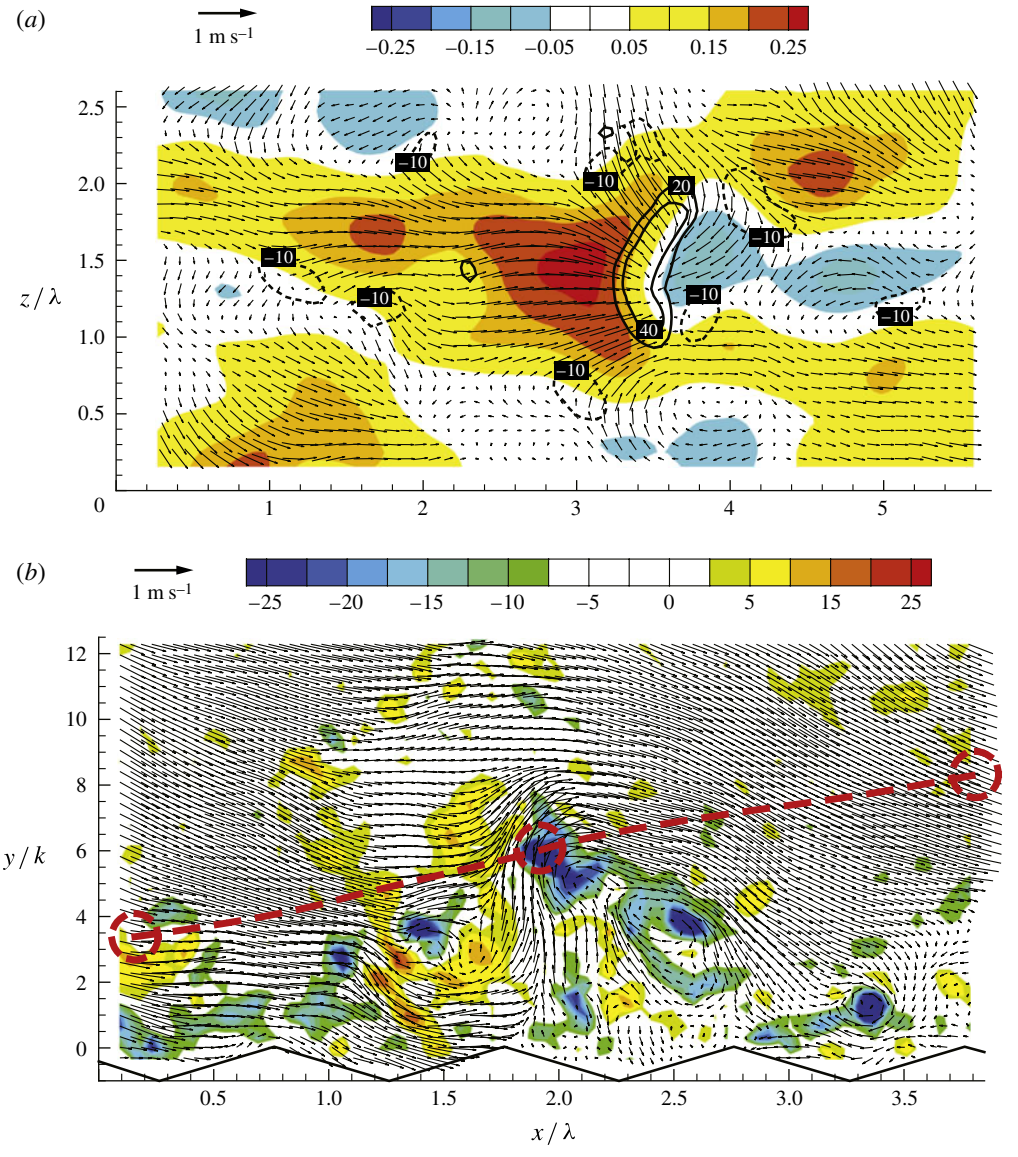

FIGURE 17. (*a*) An instantaneous sample of 3*k*-filtered velocity fluctuations, colour floods of $\widetilde{u}^{'3k}/U_c$, and black contour lines of $\Pi_{xy}^{3k}h/U_\tau^2U_c$ at $y = 1k$ showing a strong sweep impinging on the roughness. For clarity, only one in two vectors is plotted, in both directions. (*b*) An instantaneous sample of unfiltered velocity fluctuations, colour floods of unfiltered spanwise vorticity $\omega_z h/U_c$ at x–y plane showing a vortex lifting process near the wall. The dashed red line indicates the trajectory of the rising vortex across the plane.

surrounding an SGS flux peak. The sweep brings high momentum/energy flow to the vicinity of the wall, which interacts with the roughness elements, causing abrupt ejections. A plausible mechanism that produces such an ejection is introduced in the following section. Furthermore, the structures in figure 17 represent an earlier phase of the inclined vortex train formation (figure 7). The time-resolved data show that the

vortical structures in the inclined layer are ejected from a series of adjacent pyramids aligned in the streamwise direction, and consequently, are spaced by λ. These vortices typically have a negative spanwise vorticity and are generated at different times, with the one at a higher elevation ejected earlier. Although the streamwise spacing between vortices increases, presumably due to the increasing advection velocity with elevation, the vortex blob at higher elevation still consists of a bundle of roughness-scale vortices contributing to observed spectral bumps. The time-resolved data also indicate that the positive spanwise vortices are often generated from the roughness due to flow induced by negative ones transported above. Therefore, they are observed to form inclined trains underneath the region of large-scale negative vorticity as part of the same process that lifts the spanwise structures away from the wall (figure 7*b*).

3.3.2. *Mechanism for generation and transport of the coherent structures*

The existence of inclined large-scale structures with negative spanwise vorticity has been reported in a number of studies of turbulent structures over smooth walls. The formation mechanism of these structures has been attributed to the popular hairpin packet model introduced by Adrian *et al.* (2000). Although the evidence for this model is compelling for smooth-wall turbulence, we think it is less likely to occur in the present flow, especially near the wall, for the following reasons.

(i) The roughness would disrupt the formation of near-wall hairpin vortices.

(ii) In the outer layer, roughness-scale signatures are still embedded in the scales of vortices and the spacing between them.

(iii) Clear signatures of hairpin vortex packets are not present in our x–z plane data, such as elongated low-speed streaks with counter-rotating vortex pairs on both sides. We do not mean to imply that there are no low-speed regions, but that their spatial extent differs from those in smooth-wall turbulence. In fact, figure 17(*a*) shows such a low-speed area, but it is patchy and has a short streamwise extent. It should be noted that Wu & Christensen (2010) still attribute these patchy regions to low-speed streaks induced by hairpins.

(iv) In x–y planes, the counter-rotating vortices that form a pair do not have equal strength, and the negative ones are almost always stronger. As noted earlier, the time-resolved data show that the near-wall positive vortices are often induced from the roughness by the negative ones travelling above. However, in the model proposed by Wu & Christensen (2006), these pairs, referred to as retrograde and prograde vortices, result from slicing an Ω-hairpin vortex by the imaging plane, which would require the two counter-rotating vortices to have the same strength.

(v) The ejections that cause high SGS flux near the wall occur within regions of strong sweep.

To explain the phenomena observed, we propose a 'U shape', illustrated in figure 18, as the fundamental vortical structure in the present rough-wall flow. The formation of the structures is related to the roughness-induced spatial non-uniformity in the streamwise velocity distribution shown by our x–z plane data at $0 < y < 2k$ (Hong *et al.* 2011). The velocity is low along the pyramid ridgeline with a minimum above the forward face of the pyramid, and relatively high between the ridgelines. In such a domain, a predominantly spanwise vortex formed at the low-velocity regions is prone to being stretched axially by the faster streaming flow between the pyramids. Consequently, we postulate that this process generates U-shaped structures with heads along the ridgeline and legs extending forward between them. Although such a phenomenon could be associated with flow separation and vortices wrapping around

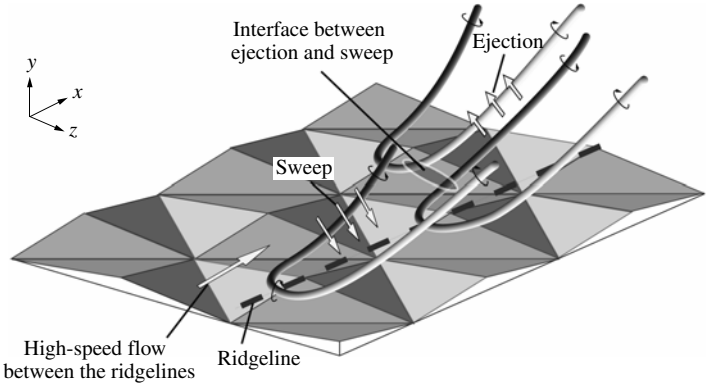

FIGURE 18. Schematics for the near-wall flow structure formation and interaction.

the roughness elements, the structures and processes described here develop above the rough surface. In reality, the quasi-streamwise legs of this structure are generally oriented asymmetrically. Nevertheless, during early phases, both counter-rotating legs have negative spanwise vorticity, and exhibit streamwise and wall-normal components of opposite sign. Imposed by the roughness geometry, these structures are initiated every $\lambda/2$ in the spanwise direction. Therefore, the minimum distance between their adjacent legs shortly after formation is less than $\lambda/2$, consistent with the p.d.f. of spacing between x–z plane counter-rotating vortices shown in figure 16. The space between two legs of the same U-shaped structure is subjected to a sweeping flow, while the ejections generated between two adjacent legs of neighbouring structures tend to lift them away from the wall. Figure 18 also illustrates how the presence of multiple structures might create the intersecting pattern of counter-rotating vortices as well as the sweep-ejection interface observed in the instantaneous and conditionally averaged distributions. The contracting flow at this sweep-ejection interface would produce strong SGS energy flux there. As noted before, intense near-wall SGS flux events frequently occur under large-scale sweeps, which bring high-momentum fluid to the wall, enhancing the strength of the U-shaped structures formed around the roughness elements. This process inherently involves direct production of SGS energy from turbulence originally at scales that are much larger than the filter size, possibly contributing to the increase in non-local energy flux near the wall (figure 4).

The distinct intersecting pattern diminishes rapidly at higher elevations as the rising legs interact with each other. However, as the spectra, p.d.f. of vortex spacing, and conditionally averaged distributions demonstrate, the roughness signature persists. In the outer layer, the significantly lower SGS energy flux is mainly produced by contraction of bundles of roughness-scale eddies within isolated remnant vortex trains. Nevertheless, these trains still maintain a preferred alignment consistent with that occurring near the wall, i.e. the positive ω_y train is more likely to be aligned in the quadrant 1–3 direction, and the negative ω_y train in the quadrant 2–4 direction. The vorticity distribution conditioned on high Π_{xz}^{3k} combines both signatures (figure 11*a*), and therefore still displays two pairs of counter-rotating vortices in the vicinity of the conditioning point, although the two trains are not present at the same time.

Using the U-shaped vortices as building blocks, a possible mechanism for the vortex train formation along with its x–y plane signatures is illustrated in figure 19. At the x–y plane aligned with the pyramid ridgeline, the time-resolved data show

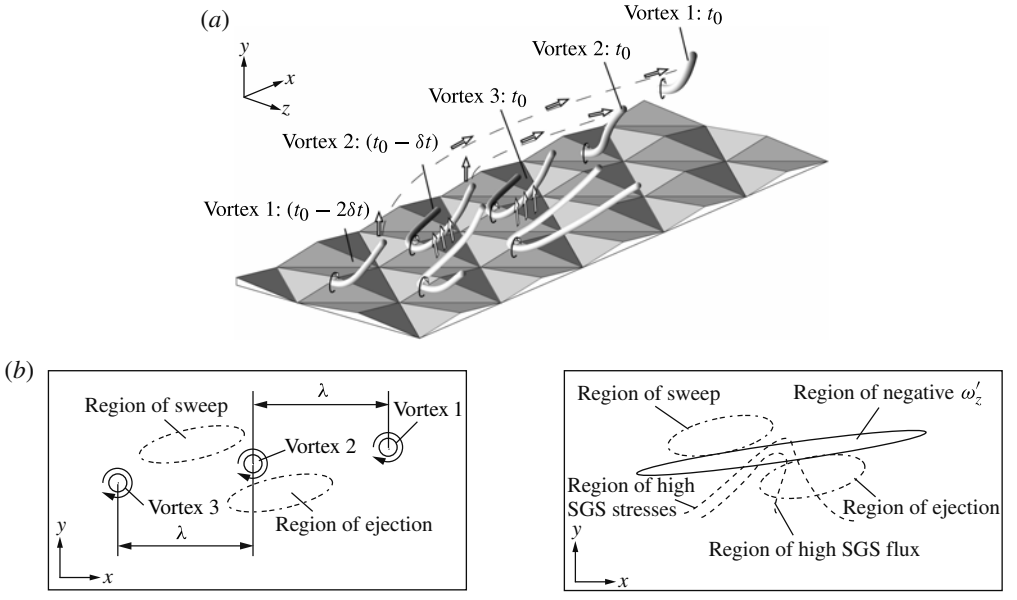

FIGURE 19. (*a*) Schematics of a possible mechanism generating a train of coherent structures (U-shaped structures) above a rough wall. (*b*) The instantaneous *x*–*y* ridgeline plane view of the inclined vortex train. (*c*) An *x*–*y* plane view of a conditionally averaged flow field based on strong SGS energy flux.

that spanwise vortices form near the pyramid crest and remain near the wall for a while. Occasionally, they rise away from the surface along trajectories similar to that presented in figure 17(*b*). As discussed earlier, although such intense events appear in a small fraction of the realizations, they dominate the SGS flux. Once the ejection-induced lifting is initiated, it involves multiple structures that are generated from different roughness elements at different times, which form an inclined vortex train. The inclination angle of this train (figure 7) and the trajectory of the rising vortex (figure 17) fluctuate around the angle of the conditionally averaged shear layer, 16° (figure 8). This lifting process could be contributed by both entrainment of large-scale outer-layer structure and ejection induced by interacting legs of neighbouring U-shaped vortices. Since the latter mechanism is supported by the near-wall time-resolved data (figure 17*b*), we would like to elaborate on this process using an illustration presented in figure 19(*a*). As an outer-layer sweep passes along the wall, the location where strong U-shaped vortices are generated shifts downstream with time. Vortex 1, i.e. the first vortex produced and lifted by the local ejection at $t_0 - 2\delta t$, is convected downstream at a faster rate than the near-wall flow along the trajectory indicated by the dashed line. Here, δt is the advection time of the large-scale sweep between two roughness elements. Vortex 2 is generated later at $t_0 - \delta t$, presumably by the same sweep. Consequently, vortex 2 lags behind and is located below vortex 1. As the sweep proceeds, it produces an inclined train of such vortices, illustrated as the three structures depicted at t_0. The resulting flow field would yield the signature sketched in figure 19(*b*) at the *x*–*y* ridgeline plane, consistent with the instantaneous sample presented in figure 7. Conditional averaging based on strong SGS flux, which captures such extreme events, would produce the distributions of vorticity, shown

in figure 19(*c*). Furthermore, as a U-shaped structure rises from the surface, the area below it becomes filled with entrained roughness-scale eddies (figures 7*a* and 17*b*), which fall in the subgrid scale in the present analysis. The SGS energy flux increases when these eddies are strained by the resolved flow, and peaks when they are subjected to the contraction at sweep-ejection interface. Consequently, it is reasonable to expect that the conditionally averaged regions of high SGS kinetic energy and flux are inclined at a steeper angle compared with that of the large-scale vortex train, consistent with figure 9(*b,e,f*). When the conditional averaging is based on the near-wall flow, one should expect that the resolved TKE peaks in the sweep region, under which the structures are more likely to be generated and lifted. The resolved TKE peak shifts to the ejection region in the outer layer as the rising structures interact and increase in scales. Accordingly, the distinct intersecting signature in the x–z plane disappears.

3.4. *Features of the SGS flow field based on the resolved turbulence*

The previous sections have shown the substantial contribution of coherent structures to the SGS energy transfer. Since LES of high Reynolds number flows does not resolve the roughness-scale phenomena, as a first step in modelling the SGS energy transfer in the presence of coherent structures we explore methods of identifying these structures using resolved quantities. Figures 20(*a*) and 20(*b*) show $3k$-filtered velocity fluctuations using conditional averaging based on high $-\partial\tilde{u}^{3k}/\partial x$ and $-\partial\tilde{u}^{3k}/\partial y$ (highest 5 %) at $y = 11k$, respectively, following the procedures described earlier in this paper. Inclined shear layers of different shapes bounded by ejection below and sweep above appear under both conditions. However, in the $\partial\tilde{u}^{3k}/\partial x$-based results (figure 20*a*), the ejection region shifts to a higher elevation downstream of the conditioning point, creating what appears to be a discontinuity in the inclined layer. The inclination of this layer upstream and downstream of the discontinuity is still $\sim 16°$, in agreement with the Π_{xy}^{3k}-based analysis. On the other hand, conditioning on $-\partial\tilde{u}^{3k}/\partial y$ (figure 20*b*) reduces the inclination angle of the shear layer locally near the conditioning point and shifts the ejection region upstream and to an area below this point. The discrepancies between the large-scale flow structures in figure 20 are imposed by the local flow features associated with each condition, which preferentially accentuates a specific region in the coherent structure. To demonstrate this point, figure 20(*c*) depicts part of the previously discussed flow, highlighting the regions of high $-\partial\tilde{u}^{3k}/\partial x$ and $-\partial\tilde{u}^{3k}/\partial y$. High $-\partial\tilde{u}^{3k}/\partial x$ develops at the transition between sweep and ejection, just upstream of the rising U-shaped vortex. Consequently, the region of highest vorticity is located downstream of the conditioning point (figure 20*a*). Conversely, high $-\partial\tilde{u}^{3k}/\partial y$ is expected to occur very near the base of the U shape, where $\tilde{\omega}_z^{3k}$ is high, and the vortex still lies in a horizontal (x–z) plane, consistent with figure 20(*b*).

The x–z plane perspectives of the $\partial\tilde{u}^{3k}/\partial x$-based conditional averaging has also been explored at both $y = k$ and $y = 11k$. The vorticity and resolved TKE maps (not shown) display trends that are similar to those obtained using Π_{xz}^{3k} or $-\tau_{11}^{3k}\tilde{S}_{11}^{3k}$ as conditioning variables (figures 11 and 12). The similar trends include the two pairs of counter-rotating vortices, the dominance shift from sweeps upstream of the conditioning point at $y = k$ to ejections downstream at $y = 11k$. These results confirm that the major characteristics of the coherent structures that are responsible for high SGS energy flux can still be captured without resolving flow features of the roughness (height) scale. The same conclusion should also hold for flow structures of scales larger than λ since

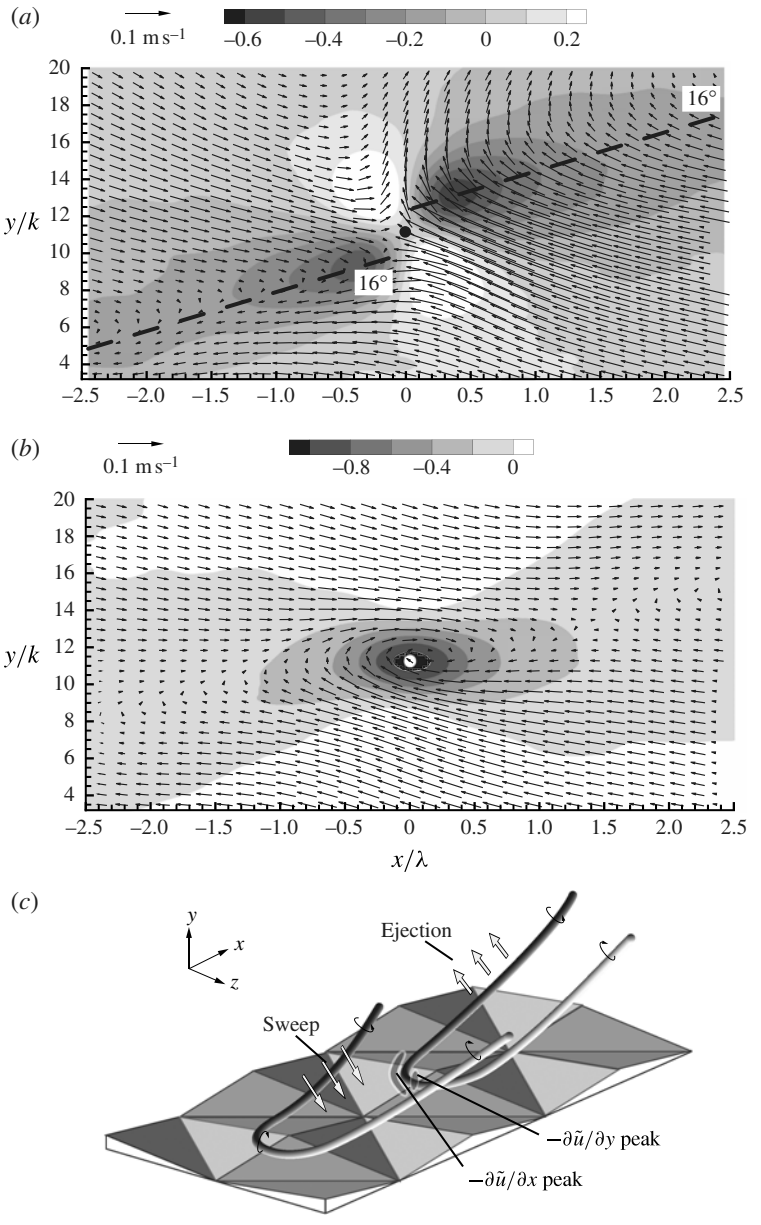

FIGURE 20. Conditionally averaged filtered velocity fluctuation and vorticity map for the highest 5 % (*a*) $-\partial\tilde{u}^{3k}/\partial x$ (*b*) $-\partial\tilde{u}^{3k}/\partial y$ at $y = 11k$. For clarity, only one in eight vectors is plotted in the horizontal direction and one in four vectors is plotted in the vertical direction. (*c*) A schematic showing peak locations of $-\partial\tilde{u}^{3k}/\partial x$ and $-\partial\tilde{u}^{3k}/\partial y$ with respect to coherent structure.

the main features of coherence structure persist in Π^{λ}_{xy}-based conditional averages (figure 14).

As discussed before, due to the presence of coherent structures, the regions of high SGS stress components do not coincide with those of the corresponding high

resolved TKE. Nevertheless, there is substantial correlation between resolved strain and SGS stress components that are spatially displaced, or even between different stress and strain components. We have investigated the cross-correlations between $\partial\tilde{u}_i^{3k}/\partial x_j$ and SGS stresses, denoted as $\rho[\partial\tilde{u}_i^{3k}/\partial x_j(x,y), \tau_{ij}^{3k}(x,y)]$, using only data conditioned on high Π_{xy}^{3k} at $(0, 11k)$, as before. Of the correlations at the same location, high values (>0.5) are only obtained along the inclined shear layer, and only for $\rho[\partial\tilde{u}^{3k}/\partial y(x,y), \tau_{11}^{3k}(x,y)]$ and $\rho[\partial\tilde{v}^{3k}/\partial y(x,y), \tau_{12}^{3k}(x,y)]$(not shown). Intriguingly, the correlation of τ_{12}^{3k} with $\partial\tilde{u}^{3k}/\partial x$ yields a much lower value (<0.2) than those with $\partial\tilde{v}^{3k}/\partial y$. This difference suggests that out-of-plane flow must play a significant role since $\partial\tilde{u}^{3k}/\partial x$ and $\partial\tilde{v}^{3k}/\partial y$ would exhibit the same trends if the flow were predominantly two-dimensional. Another notable result is the poor correlation between $\partial\tilde{u}^{3k}/\partial y$ and τ_{12}^{3k} at the same location, consistent with Liu *et al.* (1994).

As for spatially displaced strain and stress components, figure 21 presents three sample correlations between $\partial\tilde{u}_i^{3k}/\partial x_j$ at $(0, 11k)$ and the stress in the vicinity of this point. The distribution of $\rho[\partial\tilde{u}^{3k}/\partial x(0, 11k), \tau_{11}^{3k}(x,y)]$, shown in figure 21(*a*), has negative maxima that coincide with the negative vorticity peaks. This co-occurrence indicates that the SGS kinetic energy in the streamwise direction is preferentially elevated within the shear layer vortices during periods of strong streamwise contraction at the conditioning point. The positive correlation is maximum in the ejection region below the shear layer, and has a smaller peak at the edge of the sweeping area. This trend implies that when the magnitude of $\partial\tilde{u}^{3k}/\partial x$ falls above the mean value of the conditionally averaged data, i.e. the contraction is particularly strong, the stress is lower than the mean values in the ejection region, and vice versa. During high contraction events, the SGS energy is concentrated in the inclined shear layer. The high $\rho[\partial\tilde{u}^{3k}/\partial y(0, 11k), \tau_{11}^{3k}(x,y)]$ near the conditioning point, as shown in figure 21(*b*), confirms the close coupling between the resolved shear strain and the primary contributor to the SGS kinetic energy in the shear layer. The correlation between $\partial\tilde{u}^{3k}/\partial y$ and τ_{12}^{3k} (figure 21*c*) is locally quite poor. It only reaches a negative peak of $\sim$0.3 at a location about $1k$ displaced above the conditioning point. This trend seems to be a manifestation of increasing transport of subgrid momentum away from the wall with increasing strength of resolved structures.

4. Summary and discussions

Utilizing a series of high-resolution and time-resolved PIV datasets, we have investigated the SGS energy transfer among different scales in a rough-wall channel flow. Based on the energy spectra, we divide the turbulence into four scale ranges: large scales ($>6k \sim \lambda$), intermediate scales (3–6k), roughness scales (1–3k) and small scales ($<k$). The ensemble-averaged results show that with decreasing distance from the wall, there is a marked increase in the non-local SGS energy flux from scales larger than $3k$ to small scales. Moreover, the fraction of turbulence dissipated by eddies in the roughness scale is substantial in the outer layer, and is particularly high near the wall. This trend is consistent with the excessive amount of intense roughness-scale eddies that are generated near the wall and dispersed well above the roughness sublayer.

Conditional averaging is applied to investigate the flow structures that dominate energy transfer from large-scale to roughness-scale range. The analysis shows that a small fraction of the flow produces a considerable fraction of the SGS energy flux, e.g. 5 % of the flow volume generating the highest flux is responsible for 50 % of the total energy flux. In x–y planes, the conditionally averaged flow exhibits a large inclined

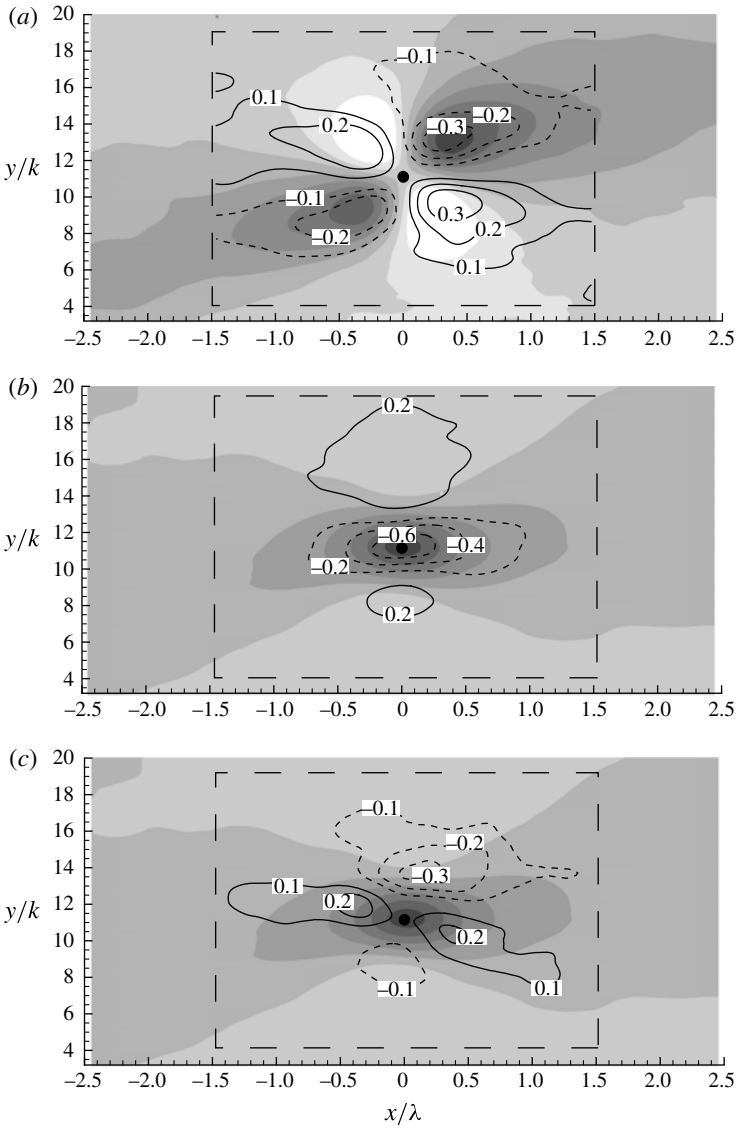

FIGURE 21. Contours of correlations between resolved velocity gradients and SGS stress components: (*a*) $\rho[\partial\tilde{u}^{3k}/\partial x(0, 11k), \tau_{11}^{3k}(x, y)]$; (*b*) $\rho[\partial\tilde{u}^{3k}/\partial y(0, 11k), \tau_{11}^{3k}(x, y)]$; (*c*) $\rho[\partial\tilde{u}^{3k}/\partial y(0, 11k), \tau_{12}^{3k}(x, y)]$. The dashed rectangles mark the region where correlations are calculated. The background for (*a*) is the conditionally averaged vorticity based on high $-\partial\tilde{u}^{3k}/\partial x$ shown in figure 20(*a*). The background for (*b,c*) is the conditionally averaged vorticity based on high $-\partial\tilde{u}^{3k}/\partial y$ shown in figure 20(*b*).

shear layer containing negative spanwise vorticity, bounded by an ejection below and a sweep above. Near the wall, the sweeping flow is dominant, while the ejection is stronger in the outer layer. In *x*–*z* planes, the conditional flow field is composed of two pairs of counter-rotating vortices that surround and induce a contracting flow at the peak of SGS flux. The direction of this flow is consistent with the location of sweep and ejection regions in *x*–*y* planes.

Examination of instantaneous realizations in the roughness sublayer reveals a flow pattern that largely agrees with the conditionally averaged results. It further shows the presence of the counter-rotating vortex pairs at the intersection of two vortex trains, each containing multiple λ-spaced vortices of the same sign. We propose a flow structure and generation mechanism that explains the observed planar signatures. The mechanism consists of the formation of U-shaped quasi-streamwise vortical structures that develop as spanwise vorticity is stretched in regions of high streamwise velocity between roughness elements. They are lifted away from the wall by the ejection resulting from other U-shaped structures generated at adjacent roughness elements. Existence of these structures has been supported recently by three-dimensional, high-resolution holographic PIV measurements (Talapatra & Katz 2012). Statistical analysis of the three-dimensional alignment of vorticity provides evidence of structures wrapping around the region of low velocity along the ridgeline. Moreover, the analysis shows that ω_z is dominant at $0 < y < k$, and the formation of elongated, sharply inclined legs due to interactions among neighbouring legs occurs predominantly at $k < y < 4k$. These results demonstrate that U-shaped structures are indeed generated above the roughness elements due to flow non-uniformities induced by the pyramids. The U-shaped structure postulated in our study bears some resemblance to the head-down hairpin vortex proposed for canopy flows in Finnigan, Shaw & Patton (2009). According to their study, these structures co-exist with the 'regular' hairpins. They postulate two mechanisms that could contribute to the generation of the head-down hairpins. The first is associated with an ejection emerging from the wall (induced by the regular hairpins) that blocks the higher-velocity flow above. The second explanation utilizes the linear stability analysis of Pierrehumbert & Widnall (1982), which attributes the formation of these structures to the mutual induction of coherent spanwise 'Stuart' vortices. Based on our study, one might also speculate that the spatial non-uniformities in streamwise velocity induced by the canopy elements contribute to the generation of the head-down hairpins.

The SGS flux typically peaks during ejection events that form under large-scale sweeps at the contracting flow interface between the sweep and ejection. As a sweeping event is transported downstream, its interaction with adjacent roughness elements at different times generates a series of ejection-induced lifting events. The resulting generation of multiple structures at different phases of development provides a plausible mechanism for inclined vortex train formation observed in the instantaneous realizations. The angle of conditionally averaged shear layer, 16°, is not significantly different from those of the sample instantaneous train and the trajectory of lifted vortices in time-resolved data. It should be noted that prior publications (e.g. Volino *et al.* 2007; Wu & Christensen 2007, 2010) attribute the inclined layer pattern over rough walls to hairpin packets, similar to smooth walls.

In the outer layer, e.g. at $y = 11k$, the SGS flux is significantly weaker than in the near-wall level, and peaks mainly within single vortex trains owing to the interaction of eddies within this structure. These trains still maintain a preferred alignment consistent with that occurring near the wall, i.e. the positive ω_y train is aligned in the quadrant 1–3 direction, and the negative ω_y train in the quadrant 2–4 direction. Therefore, the formation of two counter-rotating vortex pairs in the conditionally averaged vorticity distribution is an artifact resulting from combining vortex trains rotating in opposite directions during the conditional averaging process. In spite of the differences between structures appearing in the roughness sublayer and those of the outer layer, the roughness signature is evident in both. This signature includes a

characteristic vortex size of k, streamwise spacing of λ between vortex clusters located in a single train, and a most probable distance of 0.5λ between counter-rotating vortices in the outer layer.

The flow characteristics and distribution of SGS energy flux observed in this study inherently depend on the specific geometry and length scales of the roughness elements (k and λ) as well as their spatial arrangement. The spacing between structures and the resulting flow channelling facilitate the formation of U-shaped structures, which carry the roughness signature with them to the outer layer. Conceivably, for example, more tightly packed three-dimensional roughness elements would reduce their scale and lead to more frequent interaction between adjacent vortical structures. As a result, the local dissipation rate would be enhanced, suppressing the propagation of the roughness signatures to higher elevations. Conversely, with increasing scales of roughness elements and spacing between them, the structures that carry their signature might be able to travel farther up in the outer layer. This conjecture is consistent with the stronger roughness effect observed for turbulence over two-dimensional sparse roughness compared to flows over three-dimensional roughness provided in a number of recent studies (e.g. Lee *et al.* 2011; Volino, Schultz & Flack 2011). For surfaces with more randomly distributed roughness of varying scales (Wu & Christensen 2010), the characteristics of structures would also vary, and therefore might not yield readily detected signatures of vortex spacing and scales in energy spectra. Like some of recent turbulence studies over smooth and rough walls (e.g. Wu & Christensen 2010; Lee *et al.* 2011; Volino *et al.* 2011), the flow described in this paper contains outer-layer structures with sizes that are much larger than the characteristic roughness scales. These structures might be involved in the previously mentioned large-scale sweeping events that initiate the near-wall ejections. Many of their features are consistent with the hairpin packet model introduced by Adrian *et al.* (2000), as demonstrated in Hong *et al.* (2011). A number of publications (e.g. Krogstad & Antonia 1994; Wu & Christensen 2010) indicate that the presence of roughness reduces the streamwise extent of these large structures.

Development of SGS stress models that account for the dominant effect of coherent structures in the rough-wall turbulent flow is a great challenge. As we show, the region of high SGS kinetic energy and flux are spatially displaced from the region of high resolved TKE, i.e. the flow generating and transporting the SGS turbulence. Accordingly, some of the highest correlations occur between spatially displaced resolved velocity gradients and SGS stresses. However, since the main features of the coherent structures can be reproduced using only resolved flow parameters as a basis for conditional sampling, one hopes that improved modelling based on the filtered flow is feasible. Since a few intense structures are sufficient for generating the majority of energy flux, a workable model may be developed by introducing the proper type of inclined vortices and following a logic similar to that described by Misra & Pullin (1997) and Chung & Pullin (2009). Note that spatial displacements based on inclined structures were proposed by Piomelli *et al.* (1989) for a wall model relating wall stress to velocity. Such a model should account for the effect of roughness scales and geometry, as well as the interactions between resolved turbulence and roughness, which lead to the upsurge of SGS energy flux and stresses. This substantial increase in SGS flux near the wall is a key difference between the trends shown in the present paper and the smooth-wall boundary layer data provided by Natrajan & Christensen (2006).

Acknowledgements

This research was funded by the US Office of Naval Research under grant 000140-91-10-0-7. The programme officer is Ronald Joslin. The authors would like to thank Yuri Ronzhes for designing the new facility and Rinaldo Miorini for his assistance in operating the high-speed PIV system.

REFERENCES

ADRIAN, R. J., MEINHART, C. D. & TOMKINS, C. D. 2000 Vortex organization in the outer region of the turbulent boundary layer. *J. Fluid Mech.* **422**, 1–54.

ANDERSON, W. & MENEVEAU, C. 2010 A large-eddy simulation model for boundary-layer flow over surfaces with horizontally resolved but vertically unresolved roughness elements. *Boundary-Layer Meteorol.* **137**, 1–19.

ANTONIA, R. A. 1981 Conditional sampling in turbulence measurement. *Annu. Rev. Fluid Mech.* **13**, 131–156.

AVISSAR, R. & PIELKE, R. A. 1989 A parameterization of heterogeneous land surfaces for atmospheric numerical models and its impact on regional meteorology. *Mon. Weath. Rev.* **117**, 2113–2136.

BANDYOPADHYAY, P. R. & WATSON, R. D. 1988 Structure of rough wall turbulent boundary layers. *Phys. Fluids* **31**, 1877–1883.

BOU-ZEID, E., MENEVEAU, C. & PARLANGE, M. B. 2004 Large-eddy simulation of neutral atmospheric boundary layer flow over heterogeneous surfaces: blending height and effective surface roughness. *Water Resour. Res.* **40**, 1–18.

CARPER, M. A. & PORTÉ-AGEL, F. 2004 The role of coherent structures in subfilter-scale dissipation of turbulence measured in the atmospheric surface layer. *J. Turbul.* **5**, 1–24.

CHAMECKI, M., MENEVEAU, C. & PARLANGE, M. B. 2009 Large eddy simulation of pollen transport in the atmospheric boundary layer. *J. Aero. Sci.* **40**, 241–255.

CHEN, J., KATZ, J. & MENEVEAU, C. 2005 Implication of mismatch between stress and strain-rate in turbulence subjected to rapid straining and destraining on dynamic LES models. *J. Fluids Engng* **127**, 840–850.

CHUNG, D. & PULLIN, D. I. 2009 Large-eddy simulation and wall modelling of turbulent channel flow. *J. Fluid Mech.* **631**, 281–309.

DJENIDI, L., ANTONIA, R. A., AMIELH, M. & ANSELMET, F. 2008 A turbulent boundary layer over a two-dimensional rough wall. *Exp. Fluids* **44**, 37–47.

DORON, P., BERTUCCIOLI, L., KATZ, J. & OSBORN, T. R. 2001 Turbulence characteristics and dissipation estimates in the coastal ocean bottom boundary layer from PIV data. *J. Phys. Oceanogr.* **31**, 2108–2134.

FINNIGAN, J. J. 2000 Turbulence in plant canopies. *Annu. Rev. Fluid Mech.* **32**, 519–571.

FINNIGAN, J. J., SHAW, R. H. & PATTON, E. G. 2009 Turbulence structure above a vegetation canopy. *J. Fluid Mech.* **637**, 387–424.

FLACK, K. A., SCHULTZ, M. P. & SHAPIRO, T. A. 2005 Experimental support for Townsend's Reynolds number similarity hypothesis on rough walls. *Phys. Fluids* **17**, 035102.

GERMANO, M., PIOMELLI, U., MOIN, P. & CABOT, W. H. 1991 A dynamic subgrid scale eddy viscosity model. *Phys. Fluids* **3**, 1760–1765.

HACKETT, E. E., LUZNIK, L., NAYAK, A. R., KATZ, J. & OSBORN, T. R. 2011 Field measurements of turbulence at an unstable interface between current and wave bottom boundary layers. *J. Geophys. Res.* **116**, C02022.

HONG, J., KATZ, J. & SCHULTZ, M. P. 2011 Near-wall turbulence statistics and flow structures over three-dimensional roughness in a turbulent channel flow. *J. Fluid Mech.* **667**, 1–37.

IKEDA, T. & DURBIN, P. A. 2007 Direct simulations of a rough-wall channel flow. *J. Fluid Mech.* **571**, 235–263.

JIMÉNEZ, J. 2004 Turbulent flows over rough walls. *Annu. Rev. Fluid Mech.* **36**, 173–196.

JUNEJA, A. & BRASSEUR, J. G. 1999 Characteristics of subgrid-resolved-scale dynamics in anisotropic turbulence, with application to rough-wall boundary layers. *Phys. Fluids* **11**, 3054–3068.

KEIRSBULCK, L., LABRAGA, L., MAZOUZ, A. & TOURNIER, C. 2002 Surface roughness effects on turbulent boundary layer structures. *J. Fluids Engng* **124**, 127–135.

KHANNA, S. & BRASSEUR, J. G. 1998 Three-dimensional buoyancy- and shear-induced local structure of the atmospheric boundary layer. *J. Atmos. Sci.* **55**, 710–743.

KROGSTAD, P. Å. & ANTONIA, R. A. 1994 Structure of turbulent boundary layers on smooth and rough walls. *J. Fluid Mech.* **277**, 1–22.

KROGSTAD, P. Å. & ANTONIA, R. A. 1999 Surface roughness effects in turbulent boundary layers. *Exp. Fluids* **27**, 450–460.

KROGSTAD, P. Å. , ANTONIA, R. A. & BROWNE, L. W. B. 1992 Comparison between rough- and smooth-wall turbulent boundary layers. *J. Fluid Mech.* **245**, 599-599.

KUNKEL, G. J. & MARUSIC, I. 2006 Study of the near-wall-turbulent region of the high-Reynolds-number boundary layer using an atmospheric flow. *J. Fluid Mech.* **548**, 375–402.

LEE, J. H., SUNG, H. J. & KROGSTAD, P. Å. 2011 Direct numerical simulation of the turbulent boundary layer over a cube-roughened wall. *J. Fluid Mech.* **669**, 397–431.

LEE, S. H. & SUNG, H. J. 2007 Direct numerical simulation of the turbulent boundary layer over a rod-roughened wall. *J. Fluid Mech.* **584**, 125–146.

LESIEUR, M. & METAIS, O. 1996 New trends in large-eddy simulations of turbulence. *Annu. Rev. Fluid Mech.* **28**, 45–82.

LILLY, D. K. 1967 The representation of small-scale turbulence in numerical simulation experiments. In *The IBM Scientific Computing Symposium on Environmental Sciences*, pp. 195–210.

LILLY, D. K. 1992 A proposed modification of the Germano subgrid scale closure method. *Phys. Fluids* **4**, 633–635.

LIU, S., MENEVEAU, C. & KATZ, J. 1994 On the properties of similarity subgrid-scale models as deduced from measurements in a turbulent jet. *J. Fluid Mech.* **275**, 83–120.

MENEVEAU, C. 1994 Statistics of turbulence subgrid-scale stresses: necessary conditions and experimental tests. *Phys. Fluids* **6**, 815–833.

MENEVEAU, C. & KATZ, J. 2000 Scale-invariance and turbulence models for large-eddy simulation. *Annu. Rev. Fluid Mech.* **32**, 1–32.

MISRA, A. & PULLIN, D. I. 1997 A vortex-based subgrid stress model for large-eddy simulation. *Phys. Fluids* **9**, 2443–2454.

MONIN, A. S. & OBUKHOV, A. M. 1959 Basic laws of turbulent mixing in the surface layer of the atmosphere. *Contrib. Geophys. Inst. Acad. Sci. USSR* **24**, 163–187.

NATRAJAN, V. K. & CHRISTENSEN, K. T. 2006 The role of coherent structures in subgrid-scale energy transfer within the log layer of wall turbulence. *Phys. Fluids* **18**, 065104.

PIERREHUMBERT, R. & WIDNALL, S. 1982 The two- and three-dimensional instabilities of a spatially periodic shear layer. *J. Fluid Mech.* **114**, 59–82.

PIOMELLI, U. 1999 Large-eddy simulation: achievements and challenges. *Prog. Aerosp. Sci.* **35**, 335–362.

PIOMELLI, U. 2008 Wall-layer models for large-eddy simulations. *Prog. Aerosp. Sci.* **44**, 437–446.

PIOMELLI, U, FERZIGER, J. H., MOIN, P. & KIM, J. 1989 New approximate boundary conditions for large eddy simulations of wall-bounded flows. *Phys. Fluids* A **1**, 1061–1068.

PIOMELLI, U., YU, Y. & ADRIAN, R. J. 1996 Subgrid scale energy transfer and near wall turbulence structure. *Phys. Fluids* **8**, 215–224.

POPE, S. B. 2000 *Turbulent Flows*. Cambridge University Press.

PORTÉ-AGEL, F., MENEVEAU, C. & PARLANGE, M. B. 2000 A scale-dependent dynamic model for large-eddy simulation: application to a neutral atmospheric boundary layer. *J. Fluid Mech.* **415**, 261–284.

RAUPACH, M. R., ANTONIA, R. A. & RAJAGOPALAN, S. 1991 Rough-wall turbulent boundary layers. *Appl. Mech. Rev.* **44**, 1–25.

ROGALLO, R. S. & MOIN, P. 1984 Numerical simulation of turbulent flows. *Annu. Rev. Fluid Mech.* **16**, 99–137.

SCHULTZ, M. P. & FLACK, K. A. 2003 Turbulent boundary layers over surfaces smoothed by sanding. *J. Fluids Engng* **125**, 863–870.

SCHULTZ, M. P. & FLACK, K. A. 2007 The rough-wall turbulent boundary layer from the hydraulically smooth to the fully rough regime. *J. Fluid Mech.* **580**, 381–405.

SCHULTZ, M. P. & FLACK, K. A. 2009 Turbulent boundary layers on a systematically varied rough wall. *Phys. Fluids* **21**, 015104.

SMAGORINSKY, J. 1963 General circulation experiments with the primitive equations. *Mon. Weath. Rev.* **91**, 99–164.

TACHIE, M. F., BERGSTROM, D. J. & BALACHANDAR, R. 2000 Rough wall turbulent boundary layers in shallow open channel flow. *J. Fluids Engng* **122**, 533–541.

TACHIE, M. F., BERGSTROM, D. J. & BALACHANDAR, R. 2003 Roughness effects in low-Re_θ open-channel turbulent boundary layers. *Exp. Fluids* **35**, 338–346.

TALAPATRA, S. & KATZ, J. 2012 Coherent structures in the inner part of a rough wall boundary layer resolved using holographic PIV. *J. Fluid Mech.* (accepted).

TOWNSEND, A. A. 1976 *The Structure of Turbulent Shear Flow*. Cambridge University Press.

VAN HOUT, R., ZHU, W., LUZNIK, L., KATZ, J., KLEISSL, J. & PARLANGE, M. 2007 PIV measurements in the atmospheric boundary layer within and above a mature corn canopy. Part 1. Statistics and energy flux. *J. Atmos. Sci.* **64**, 2805–2824.

VOLINO, R. J., SCHULTZ, M. P. & FLACK, K. A. 2007 Turbulence structure in rough- and smooth-wall boundary layers. *J. Fluid Mech.* **592**, 263–293.

VOLINO, R. J., SCHULTZ, M. P. & FLACK, K. A. 2011 Turbulence structure in boundary layers over periodic two- and three-dimensional roughness. *J. Fluid Mech.* **676**, 172–190.

WU, Y. & CHRISTENSEN, K. T. 2006 Population trends of spanwise vortices in wall turbulence. *J. Fluid Mech.* **568**, 55–76.

WU, Y. & CHRISTENSEN, K. T. 2007 Outer-layer similarity in the presence of a practical rough-wall topography. *Phys. Fluids* **19**, 085108.

WU, Y. & CHRISTENSEN, K. T. 2010 Spatial structure of a turbulent boundary layer with irregular surface roughness. *J. Fluid Mech.* **655**, 380–418.